Mineralium Deposita (2019) 54:1243–1264
https://doi.org/10.1007/s00126-019-00872-w

ARTICLE

In situ LA–ICP–MS trace element analyses of magnetite: genetic implications for the Zhonggu orefield, Ningwu volcanic basin, Anhui Province, China

Weian Sun[1,2] · Feng Yuan[1,2,3] · Simon M. Jowitt[4] · Taofa Zhou[1,2] · Guangxian Liu[1,2] · Xiaohui Li[1,2] · Fangyue Wang[1,2] · Valentin R. Troll[5]

Received: 11 May 2017 / Accepted: 26 February 2019 / Published online: 23 March 2019

Abstract

The Zhonggu orefield is located within the southern Ningwu volcanic basin and is one of the largest iron ore districts within the Middle–Lower Yangtze River Metallogenic Belt (MLYRMB) of eastern China. The area hosts the Gushan iron oxide–apatite (IOA) deposit and the Baixiangshan, Longshan, Hemushan, Zhongjiu, and Taipingshan skarn-type iron deposits. Here, we employ laser ablation–inductively coupled plasma–mass spectrometry (LA–ICP–MS) to determine trace element concentrations in magnetite from these deposits. Combining these new data with geological information from these deposits indicates that the iron ore within the Gushan deposit has V and Ti compositions that are strongly suggestive of a Kiruna-type IOA origin. Specifically, the V and Ti chemistry of magnetite in iron ore breccias from the Gushan deposit suggests that this style of mineralization formed at a high temperature and as a result of magmatic magnetite precipitation. This was followed by precipitation of lower temperature magmatic–hydrothermal massive magnetite. Both types of magnetite host exsolved ilmenite. Elemental mapping also indicates that Gushan breccia-hosted magnetite records hydrothermal fluid activity that formed late-stage vein mineralization. In comparison, other deposits within the Zhonggu orefield all contain magnetite with compositions that are indicative of skarn mineralization. This implies that these deposits formed as a result of magmatic–hydrothermal rather than purely magmatic or purely hydrothermal activity, contrasting with the Gushan deposit. Finally, the geochemistry of magnetite within thick anhydrite units in the Longshan deposit indicates the formation by low-temperature sedimentary processes, and this magnetite was subsequently overprinted as a result of hydrothermal activity during the formation of the main Longshan deposit. Overall, this study indicates that the IOA, skarn-type, and sedimentary anhydrite-type iron mineralization in the Zhonggu iron ore field record evolving metallogenic processes from initially orthomagmatic mineralizing systems to high- to moderate-temperature magmatic–hydrothermal systems and finally to low-temperature hydrothermal mineralization.

Keywords Zhonggu orefield · LA–ICP–MS · Trace elements · Kiruna · Iron oxide–apatite · Skarn

Editorial handling: J. Mungall

Electronic supplementary material The online version of this article (https://doi.org/10.1007/s00126-019-00872-w) contains supplementary material, which is available to authorized users.

✉ Feng Yuan
yf_hfut@163.com

1 School of Resources and Environmental Engineering, Hefei University of Technology, Hefei 230009, China

2 Anhui Province Engineering Research Center for Mineral Resources and Mine Environments, Hefei University of Technology, Hefei 230009, Anhui, China

3 Xinjiang Research Centre for Mineral Resources, Xinjiang Institute of Ecology and Geography, Chinese Academy of Sciences, Urumqi 830011, Xinjiang, China

4 Department of Geoscience, University of Nevada Las Vegas, 4505 S. Maryland Parkway, Las Vegas, NV 89154-4010, USA

5 Department of Earth Sciences, Section for Mineralogy, Petrology and Tectonics (MPT), Uppsala University, Villavägen 16, SE-75236 Uppsala, Sweden

Introduction

The Middle–Lower Yangtze River Metallogenic Belt (MLYRMB) of eastern China hosts significant amounts of Cu, Au, Mo, and Fe mineralization, making it one of the most important regions for mineral exploration in China. More than 200 mineral deposits, within seven separate ore districts, have been identified in this region (Zhou et al. 2008, 2012; Jiang et al. 2010; Wang et al. 2011; Yang et al. 2017). The Ningwu iron district is the largest district within the MLYRMB and contains several orefields, including Zhonggu. This orefield contains several iron deposits, including the Baixiangshan, Longshan, Hemushan, Zhongjiu, and Taipingshan deposits. These deposits were originally labeled porphyry-type iron deposits by Chinese researchers (Ningwu Research Group 1978) and are all temporally and spatially related to local intermediate–mafic magmatic rocks. In addition, this area also hosts the Gushan iron deposit, which contains magnetite–apatite and hematite–apatite ore that is generally free of hydrothermal alteration. This led some researchers to suggest that this deposit is a Kiruna-type iron oxide–apatite (IOA) deposit (Hou et al. 2009, 2010; Yuan et al. 2010). The genetic concepts for Kiruna-type IOA deposits are broadly split into magmatic and hydrothermal replacement-type models. The former involves dominantly orthomagmatic processes such as magmatic crystallization, crystal segregation, and the high-temperature exsolution of magmatic fluids to generate intrusive and extrusive iron ores as a result of high-temperature magmatic activity (Frietsch 1978; Lundberg and Smellie 1979; Pollard 2000; Nyström et al. 2008; Tornos et al. 2011; Jonsson et al. 2013; Westhues et al. 2016, 2017). In comparison, the hydrothermal model for Kiruna-type IOA mineralization (Paràk 1975, 1984; Hitzman et al. 1992; Ali et al. 1996; Rhodes and Oreskes 2009; Sillitoe and Burrows 2002; Ghasem and Majid 2013) involves hydrothermal replacement or precipitation at temperatures < 600 °C. These IOA deposits may represent the deep roots of iron oxide–copper–gold (IOCG) systems, based on magnetite and associated pyrite isotopic and trace element data for the Los Colorados IOA deposit in northern Chile (Knipping et al. 2015a, b; Reich et al. 2016), although other researchers discount the link between IOA and IOCG systems (e.g., Groves et al. 2010). Similar magmatic (Song et al. 1981; Hou et al. 2009, 2011; Li et al. 2014; Jiang 2015) and hydrothermal (Lu et al. 1990; Gu and Ruan 1988, 1990) models have been proposed for the Gushan deposit, indicating that the genesis of this deposit remains unresolved. All of the deposits in the study area are closely related to intermediate–mafic intrusions that formed contemporaneously from magmas derived from a single source and underwent similar magmatic evolutionary processes (Yuan et al. 2014; Sun et al. 2017). However, the genetic relationship between individual deposits in the study area remains unclear. For example, it is currently unknown whether and how the formation of the Kiruna IOA-type Gushan deposit is linked to the magmatic–hydrothermal mineralizing activity recorded elsewhere in the Zhonggu iron orefield. Lastly, the Longshan deposit hosts poorly understood magnetite mineralization that is hosted by a massive, and thick, bedded anhydrite unit.

A number of studies report magnetite chemistry from banded iron formations (BIF), Kiruna-type IOA deposits, magmatic Fe–Ti oxide deposits, and Fe skarn deposits (Dupuis and Beaudoin 2011; Huberty et al. 2012; Nadoll et al. 2012), as well as within IOCG and porphyry Cu–Au (Huang et al. 2018) systems. Magnetite contains trace amounts of Al, Ti, V, Si, Ca, Mn, and Mg (Dupuis and Beaudoin 2011; Nadoll et al. 2012), and the concentrations and ratios of these elements can provide insights into the different processes that form magnetite. Thus, magnetite trace element concentrations can be used to fingerprint and differentiate between different types of mineral deposits (Carew 2004; Singoyi et al. 2006; Beaudoin et al. 2007; Rusk et al. 2009; Dare et al. 2012; Nadoll et al. 2012, 2014a, b; Boutroy et al. 2014). Variations in the geochemical properties of magnetite are believed to reflect changes in physicochemical conditions (Dupuis and Beaudoin 2011), including fluid compositions and changes in temperature, pressure, and oxygen and sulfur fugacity conditions (Nadoll et al. 2012). This means that magnetite compositions can both constrain the physicochemical conditions of mineralization and also differentiate between different types of mineral deposit (Dupuis and Beaudoin 2011; Zhao et al. 2016).

Here, we present the results of laser ablation–inductively coupled plasma–mass spectrometry (LA–ICP–MS) determination of the concentrations of a large suite of trace and rare earth elements (REE) within magnetite from a number of different iron deposits within the Zhonggu orefield. These data enable the geochemical characterization and comparison of magnetite from different types of deposit and provide insights into the processes that formed the different styles of mineralization. The results therefore provide insights into the genetic links between the deposits in this region and the processes that generate different types of iron ore deposits.

Geological background

The MLYRMB is located on the northern margin of the Yangtze Block to the south of the Qinling–Dabie orogenic belt and the North China Craton. The Middle–Lower Yangtze River valley contains pre-Sinian metamorphic basement rocks (~ 1.7 Ga, Yang et al. 1987; Chang et al. 1991), Sinian (870–500 Ma) clastic rocks, dolomite and chert, widespread Cambrian to Early Triassic carbonate sedimentary successions, Jurassic continental clastic rocks, and Cretaceous continental volcanic rocks intercalated with red bed sedimentary rocks. It is bounded by the Yangxing–Changzhou Fault to the southeast, the Tan–Lu Fault to the northwest, and to the north by the Xiangfan–Guangji Fault (Fig. 1). The belt

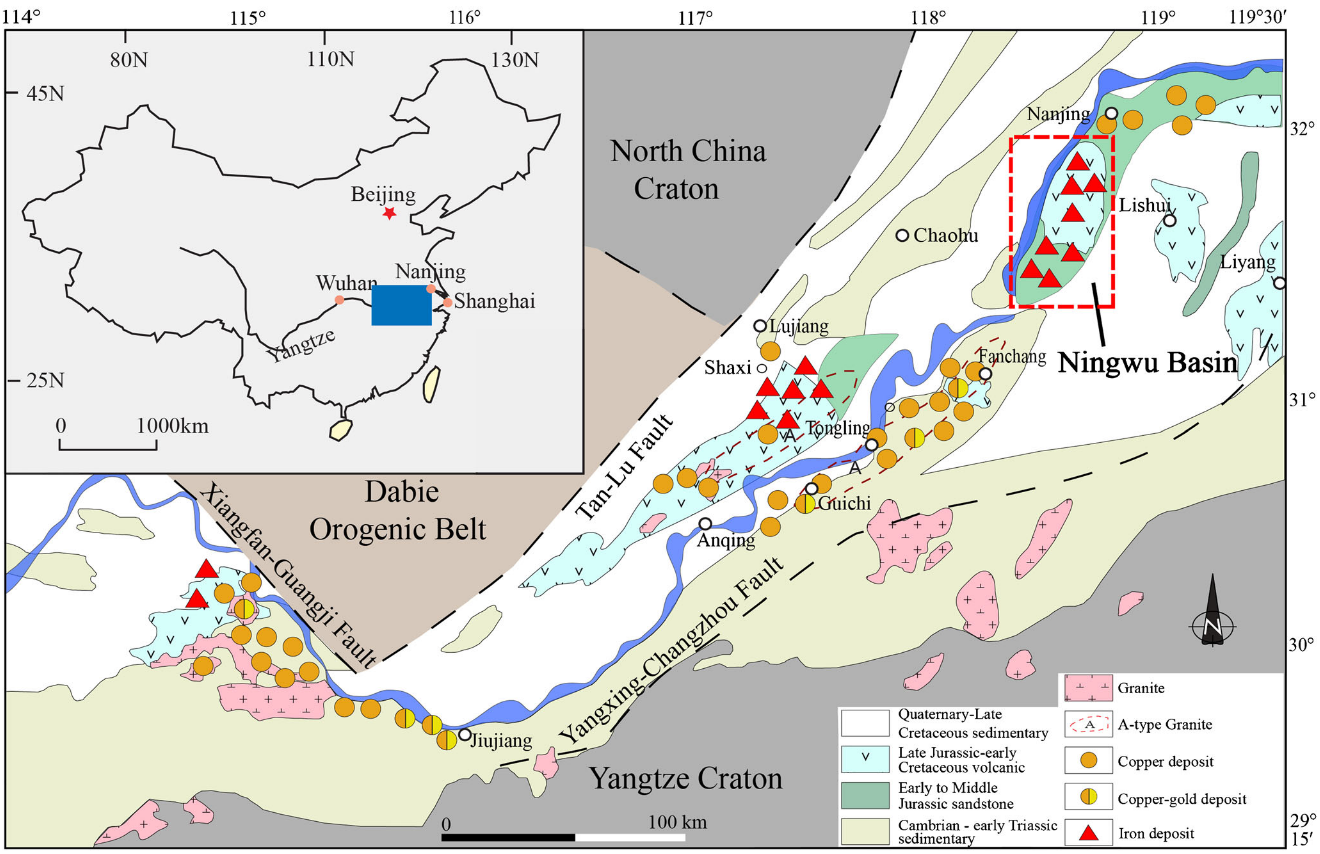

Fig. 1 Geological map showing the location of ore deposits and associated igneous rocks in the Middle–Lower Yangtze River Valley Metallogenic Belt (modified after Chang et al. 1991; Mao et al. 2011)

contains major E–W and NNE–SSW trending faults that controlled both magmatism and the distribution of mineral deposits (Zhai et al. 1992). Magmatism and mineralization in the study area is closely related to the Jurassic–Cretaceous Yanshanian tectonic and magmatic event (Fig. 1), which generated a series of uplifted blocks and fault-bound basins; multiple stages of explosive, effusive, and intrusive magmatism; and voluminous polymetallic Cu, Mo, Fe, and Au mineralization. The mineral deposits are divided into the Edong, Jiurui, Anqing–Guichi, Luzong, Tongling, Ningwu, and Ningzhen ore districts (Fig. 1).

Geology of the Ningwu Basin

The Mesozoic Ningwu continental volcanosedimentary basin is located along the northern margin of the Yangtze Block within the eastern MLYRMB (Pan and Dong 1999; Fig. 2). The basin is partially filled by continental volcanic rocks that have been intruded by cogenetic subvolcanic to plutonic rocks. It is bounded by the NNE–SSW trending Yangtze fault, the NNE–SSW trending Fangshan–Nanling fault, the NW–SE trending Nanjing–Hushu fault, and the NW–SE trending Wuhu fault. The basement of the volcanic basin is dominated by sedimentary rocks of the Middle Triassic Zhouchongcun and Triassic Huangmaqing formations, the Lower–Middle Jurassic Xiangshan Group, and the Upper Jurassic Xihengshan Formation. The volcanic sequence within the basin is divided from bottom to top into the Longwangshan (~ 20% of the volcanic rocks), Dawangshan (~ 70%), Gushan (~ 5%), and Niangniangshan (~ 5%) formations, with the Niangniangshan Formation only cropping out in the Niangniangshan area within the central part of the basin (Fig. 2). Zircon LA–ICP–MS U–Pb dating of the volcanic rocks yielded consistent Early Cretaceous ages (Zhou et al. 2011), and the dioritic intrusions within the basin are geochemically similar to the volcanic rocks of the Dawangshan Formation that host these intrusive rocks. The Ningwu Basin contains (from north to south) the Meishan, Washan, and Zhonggu orefields, which host iron deposits associated with magmatic rocks.

Geology and mineral deposits of the Zhonggu orefield

The Zhonggu orefield is located in the southern part of the Ningwu volcanic basin (Fig. 3). The area records intense folding and faulting as well as voluminous magmatism. The mineralizing and magmatic events were spatially controlled by NNE–SSW and WNW–ESE trending faults. The orefield

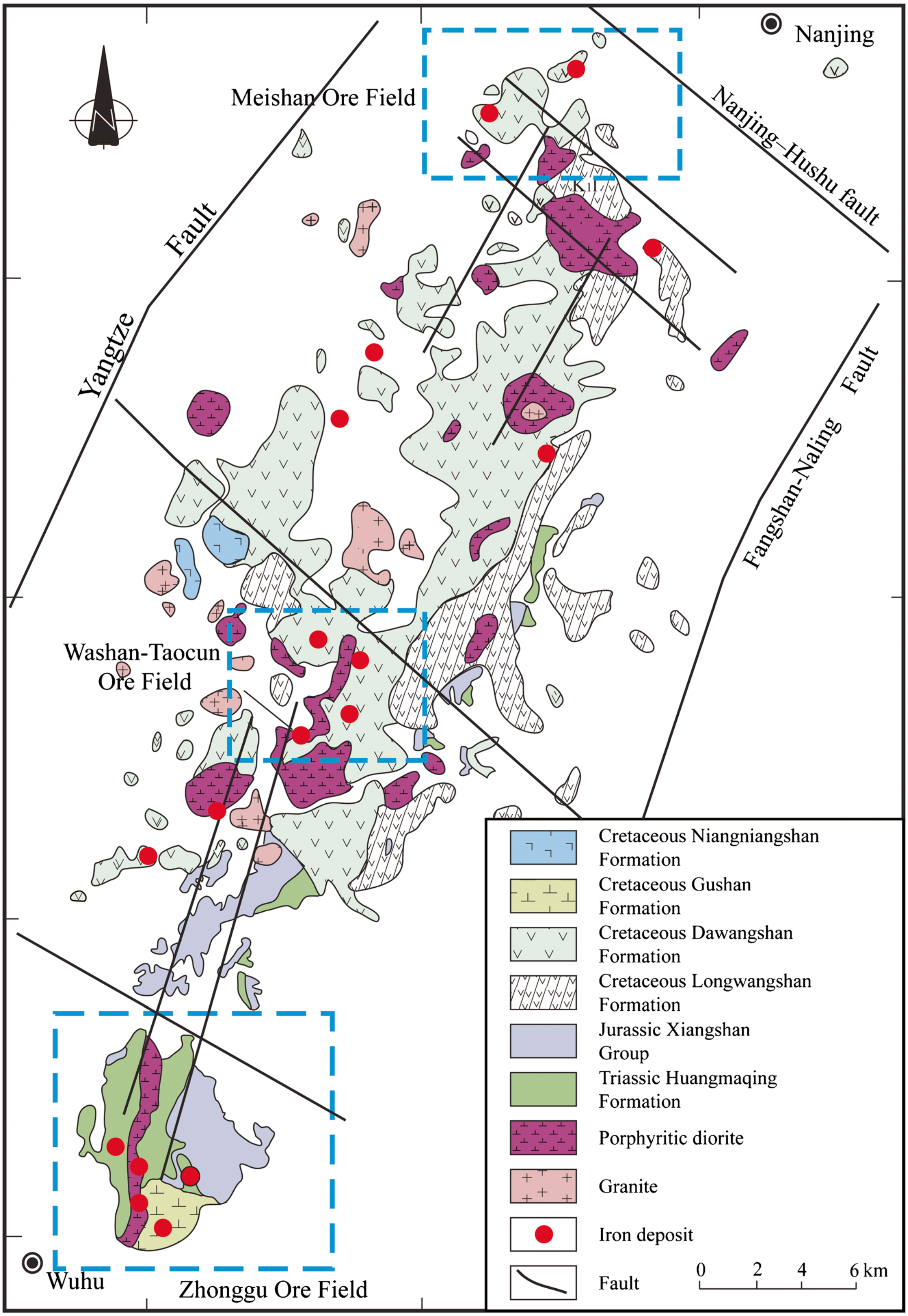

Fig. 2 Geological map showing the Ningwu Basin main geological units, major faults, and the location of major mineral deposits within Ningwu Basin (modified after Ningwu Research Group 1978)

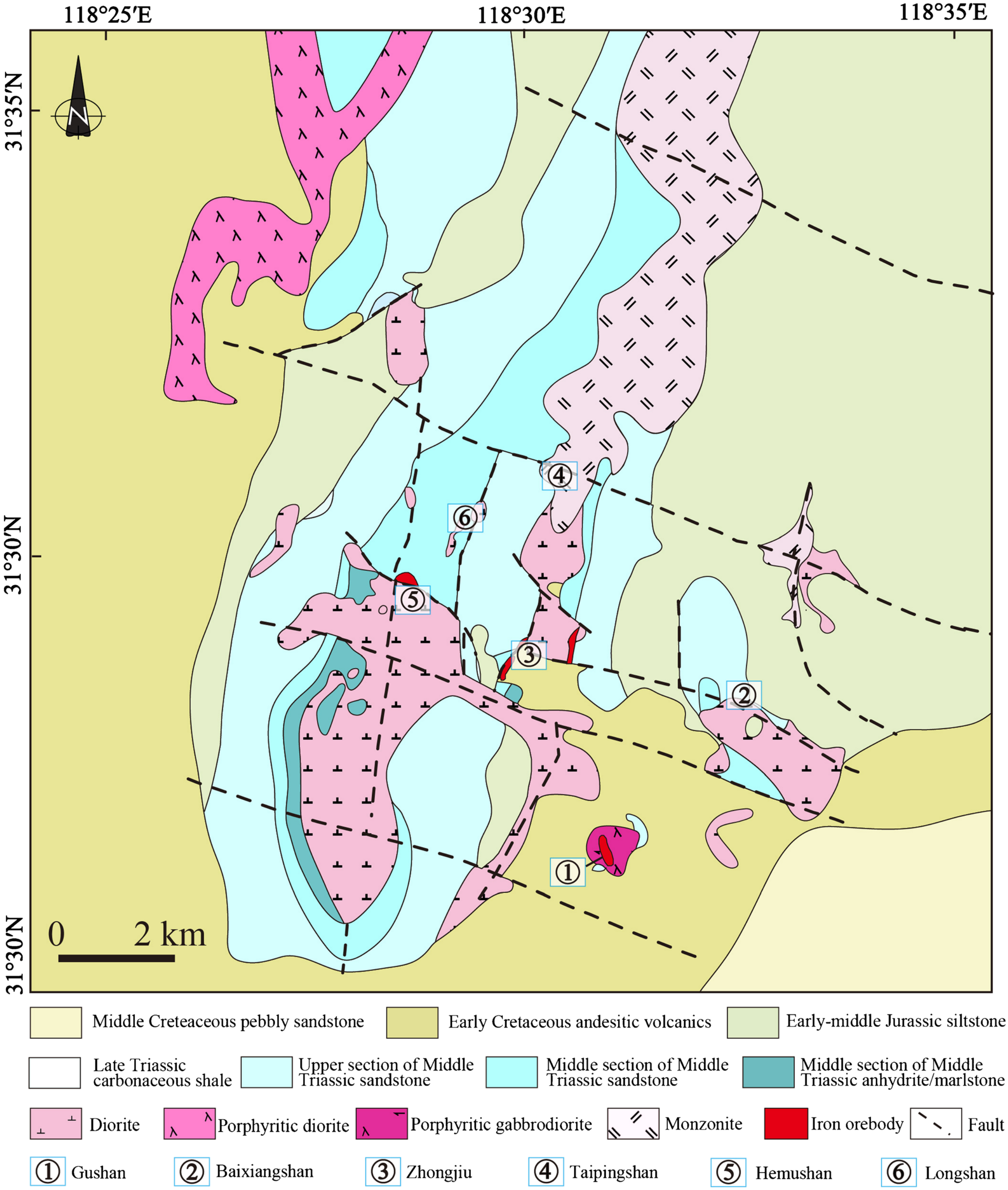

Fig. 3 Geological map of the Zhonggu orefield, showing major lithological units and intrusions and the location of key mineral deposits and faults (modified after Sun et al. 2017)

contains a sedimentary basement sequence that is subdivided into the Middle Triassic Zhouchongcun anhydrite/marlstone and Huangmaqing sandstone formations on one side and siltstones of the Lower–Middle Jurassic Xiangshan Group on the other (Fig. 3). In total, the Zhonggu orefield contains > 800 Mt of iron mineralization (Sun et al. 2017).

Gushan deposit

The Gushan deposit is an open pit mine producing magnetite–hematite–apatite iron ore. The deposit is hosted by a caldera associated with andesitic volcanic rocks and a porphyritic gabbrodiorite intrusion (Fig. 4). The porphyritic gabbrodiorite crops out over an area of 5 km^2 and was emplaced into brecciated sandstone, muddy siltstone, and shale units of the Triassic Huangmaqing Formation. Mineralization occurs both within the intrusion and in brecciated zones along the contact between the intrusion and the surrounding sandstone and shale units (Yuan et al. 2014; Jiang 2015; Fig. 4). The deposit has

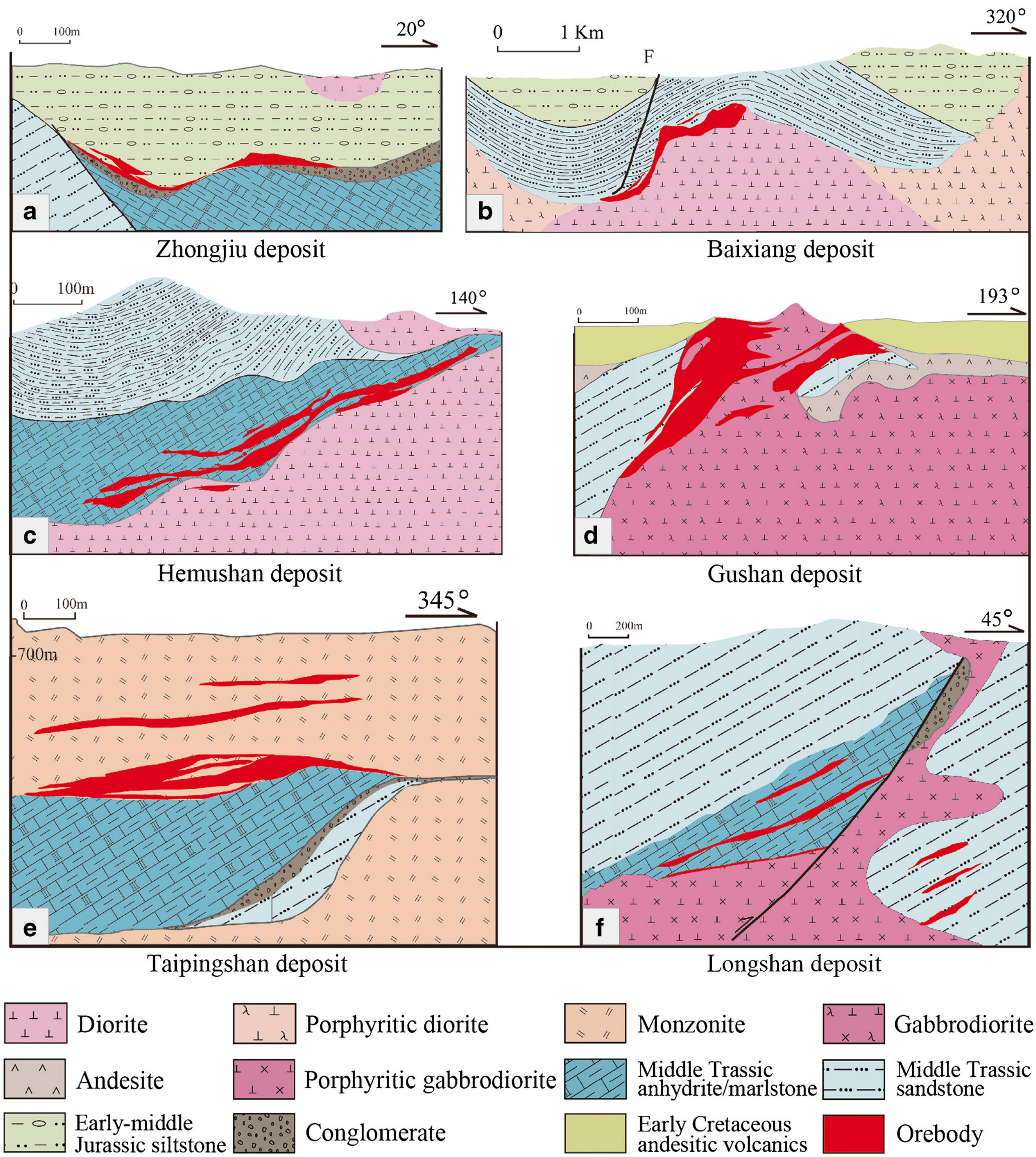

Fig. 4 Geological cross-sections through the Zhonggu Fe deposits (modified after Ningwu Research Group 1978). **a** Zhongjiu deposit. **b** Baixiangshan deposit. **c** Hemushan deposit. **d** Gushan deposit. **e** Taipingshan deposit. **f** Longshan deposit

produced ~ 180 Mt of iron ore at grades of 50–60 wt% Fe_3O_4, with high grade ores having grades of 80 wt% Fe_3O_4. The orebodies are ring-shaped in the east, but are irregularly shaped in the west, and the southwestern part of the deposit contains NE–SW trending vein orebodies.

The deposit contains brecciated, massive, and vein iron mineralization, with the former two types forming 80% of the total iron resource. The breccia-hosted mineralization within the deposit consists of fragments of shale and sandstone country rock cemented by magnetite (Fig. 5a). The iron ore breccias also contain clasts that appear to define chimney-like vents, possibly reflecting the movement of ore-forming magmatic–hydrothermal or hydrothermal fluids in this area (Fig. 5d, e). These breccias transition into massive iron mineralization along gradual contacts (Fig. 5f), contrasting with the sharp boundaries of the vein-hosted iron ore. Approximately 40% of the deposit consists of lenses and irregularly shaped bodies of massive magnetite. Vein-hosted iron ore commonly cross-cuts both massive and breccia-hosted iron ores as well as the surrounding country rock (Fig. 5i). The vein-hosted ores contain magnetite intergrown with euhedral apatite that contains abundant fluid inclusions (Fig. 5j). Some of this apatite within the vein-hosted ores has weathered out, leaving voids that were later filled by α-quartz (Fig. 5j, k). The deposit records minor late-stage hydrothermal oxidation that transformed the rims of individual magnetite crystals to hematite, especially within the upper parts of the orebodies (Fig. 5h). The ore records later supergene alteration associated with the development of jasper. The deposit is dominated by magnetite–hematite–apatite, magnetite–apatite–siderite, hematite–quartz, and calcite–chalcedony assemblages associated with silicification and kaolin and carbonate alteration. Apatite is present within all three ore types but seems more abundant in the vein-hosted iron ore (Fig. 5j).

The samples analyzed from the Gushan deposit include two iron ore breccia samples (gk-29 and A-35; Fig. 5a), two massive ore samples (gs-3 and gs-16; Fig. 5g), and two vein-hosted ore samples (gs-32 and gk-30; Fig. 5i).

Other deposits in the Zhonggu orefield

The other deposits within the Zhonggu orefield, namely the Longshan, Taipingshan, Baixiangshan, Zhongjiu, and Hemushan deposits, are located in areas containing Triassic sandstone and muddy limestone units (Fig. 4). These units are associated with zoned alteration and minor amounts of mineralization that increase in abundance with proximity to the ore-related intrusions (Fig. 6a), with the majority of iron orebodies located along the contact between muddy limestones and intrusions. Unaltered portions of the intrusions contain idiomorphic diopside, amphibole, and actinolite. Alteration associated with iron ore formation is widespread (Fig. 6d, e), and plagioclase has frequently undergone albitization (Fig. 6c). This ore-related alteration formed diopside, albite, and epidote, with this alteration most pronounced near the contact with the muddy limestone (Fig. 6b, c). The iron ore mineralization consists of magnetite intergrown with phlogopite along with lesser amounts of epidote and chlorite (Fig. 6f, h–j). The paragenesis of this alteration is shown in Fig. 6g, where diopside has been replaced by phlogopite, and then phlogopite has been replaced by chlorite. The mineralization also records some postmineralization carbonate and clay mineral alteration (Fig. 6j). The magnetite is typically disseminated, forming small anhedral crystals (Fig. 6i, j) that are in some cases replaced by postmineralization pyrite and/or kaolin (Fig. 6k, l). All stages of mineralization and postmineralization alteration are associated with anhydrite that, with the exception of the Gushan deposit, is intergrown with diopside, amphibole, epidote, and magnetite, indicating a common anhydrite formation event (Fig. 6d, f, g). In addition, drilling around the Longshan deposit identified thick evaporite units dominated by anhydrite, with minor amounts of rounded magnetite that yielded Fe_3O_4 grades of 15–25 wt%. The characteristics of each deposit are summarized in Table 1.

The samples from the Longshan deposit included two disseminated (LS401-439 and LS0028, Fig. 6j) and one anhydrite formation-hosted (LS002-910, Fig. 6m) iron ore samples. Representative disseminated ore samples from the Hemushan (HM2501-682), Taipingshan (TP402-49 and TP003-24, Fig. 6k), Zhongjiu (ZZK-6 and ZZK-22), and Baixiangshan (BX3304 and BX3709) deposits were also analyzed during this study.

Analytical techniques

Mineral major and minor element compositions were determined by EMPA employing a JEOL JXA 8230 electron microprobe at the School of Resources and Environment Engineering, Hefei University of Technology, Hefei, China. We used a 15-kV accelerating voltage, a beam current of 20 nA, an electron beam size of 5 μm, and 10–20 s peak counting times. The samples were also imaged using backscattered electron (BSE) imaging prior to quantitative EPMA. The analyses were calibrated using natural and synthetic mineral standards as follows: spinel for Mg and Al, diopside for Si, ilmenite for Ti, chromite for Cr and Fe, manganese oxide for Mn, niccolite (NiAs) for Ni, sphalerite for Zn, albite for Na, and phlogopite for K. Iron was determined as total iron (FeO_t), and Fe^{2+} and Fe^{3+} were calculated by assuming an $R^{2+}R^{3+}{}_2O_4$ formula and balancing RO: R_2O_3 = 1 for magnetite. The results of these analyses are given in ESM 1, and EPMA-derived Fe concentrations were used for internal standardization during laser ablation–inductively coupled plasma–mass spectrometry (LA–ICP–MS) analysis and data reduction.

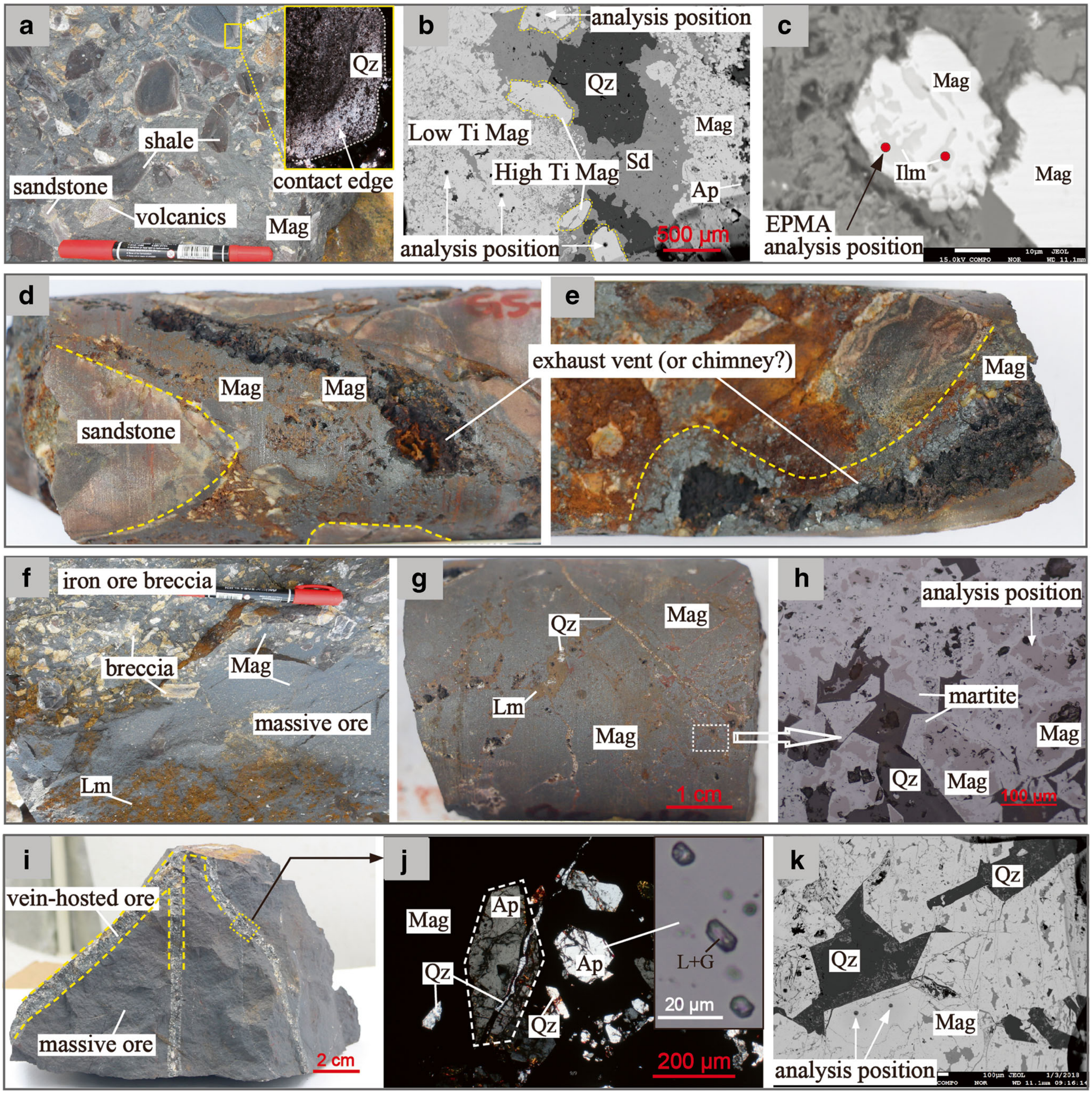

Fig. 5 Representative photographs and photomicrographs of samples from the Gushan deposit. **a** Iron ore breccia and associated photomicrograph (cross-polarized light) showing the edge of this breccia. **b** BSE image of high- and low-Ti magnetite within the iron ore breccia; black pits show the location of LA–ICP–MS analyses. **c** Exsolution of ilmenite (gray) from magnetite (light gray). **d**, **e** Exhaust vent or chimney (?) within iron ore breccia. **f** Contact between iron ore breccia and massive iron ore. **g** Representative example of massive iron ore. **h** Massive magnetite with martite rim shown under reflected light. **i** Vein-hosted iron ore cross-cutting earlier-formed massive ore. **j** Automorphic apatite intergrown with magnetite cross-cut by later quartz and apatite containing fluid inclusions. **k** BSE image showing magnetite and α-quartz filling voids left by the alteration and removal of apatite. Abbreviations: Mag = magnetite, Ap = apatite, Qz = quartz, Lm = limonite, Sd = siderite, Ilm = ilmenite; L = liquid phase fluid inclusion, L + G = liquid + gas phase fluid inclusion

Magnetite trace element compositions were determined using LA–ICP–MS analysis of polished thick sections at the In Situ Mineral Geochemistry Lab, Ore Deposit and Exploration Centre (ODEC), Hefei University of Technology, Hefei, Anhui Province, China. These analyses were undertaken using an Agilent 7900 Quadrupole ICP–MS coupled to a Photon Machines Analyte HE 193-nm ArF Excimer Laser Ablation system equipped with a SQUID signal smoothing device. Helium was used as a carrier gas and was mixed with argon used as a makeup gas via a T-connector before entering the ICP. Each analysis used a uniform spot size diameter of 30 µm at a laser pulse frequency of 8 Hz and with a laser energy of ~2 J/cm^2 for 40 s after measuring a gas blank for 20 s (ESM 2 and 4). Standard reference materials GSE-1g, GSC-1g, BCR-2G, and NIST 612 were used as external standards to plot calibration curves using preferred element concentrations for the USGS reference glasses from the GeoReM database (http://georem.mpch-mainz.gwdg.de/). Off-line data processing was undertaken using the ICPMS Data Cal software package (Liu et al. 2008), and trace element compositions of oxide minerals were calibrated against multiple reference materials using ^{57}Fe for internal standardization. The analytical uncertainties of the major and trace elements determined during this study are 5 and 10%, respectively, with the uncertainties on the major element compositions of magnetite and hematite determined by LA–ICP–MS being 5% or less. Individual magnetite grains were analyzed within each sample and some grains were analyzed twice.

In addition to these spot analyses, the compositional variations within single magnetite crystals in thick sections of iron ore breccia (A23) and massive ore (gs-16) samples from the Gushan deposit were also determined by elemental LA–ICP–MS mapping. These multi-element analyses yielded results expressed in counts per second (CPS) to give relative elemental abundances and the resulting data were processed using the Matlab LIMS data processing software package, yielding color-coded maps showing the distribution of elements within this sample. All of the resulting data are given in ESM 3.

Results

Iron ores from the Gushan deposit

The major element analysis of magnetite by EMPA from the iron ore breccia (Gushan-B), massive iron ore (Gushan-M), and vein-hosted iron ore (Gushan-V) from the Gushan deposit included a number of elements (CaO, Na_2O, SiO_2, and NiO) with concentrations below the limits of detection (LOD). Almost all MgO, Al_2O_3, and TiO_2 concentrations are above 0.02 wt% and the results are given in ESM 1. The majority of the magnetite in these samples contain < 1 wt% TiO_2, although some magnetite within the iron ore breccias contains higher concentrations (4.1–9.5 wt% TiO_2). BSE imaging of these magnetites indicates that they are subhedral, contrasting with the smaller and lower TiO_2 magnetite in the iron ore breccia (Fig. 5b). However, beyond this difference in grain size and shape, we detected few other visible differences between high- and low-Ti magnetite during BSE imaging. High-magnification BSE imaging did identify grid-patterned ilmenite lamellae within high-Ti magnetite (Fig. 5c). These ilmenites contain 42.5–49.5 wt% TiO_2 as determined by using a focused 3-µm electron beam.

The LA–ICP–MS analysis of magnetite within the Gushan-B iron ore breccia samples yielded fairly uniform concentrations of Mg, Al, V, Ti, and Ga but variable concentrations of Ca, Zn, Ni, and Ti. These concentrations differ by up to almost an order of magnitude, as exemplified by Ca concentrations (12–619 ppm; ESM 2; Fig. 7). Only minor compositional differences are present between massive and vein-hosted magnetite within other deposits in the study area. Both of these types of magnetite contain similar concentrations of Mg, Cr, V, Ti, Co, Ni, and Zn but variable amounts of Ca and Al (ESM 2). The correlations between the concentrations of these elements are shown in Fig. 8. Elemental mapping of magnetite within the Gushan iron ore breccia sample identified core-to-rim compositional variations (Fig. 9). In addition, BSE imaging identified fracturing within the magnetite as well as metasomatic rims that are both associated with minor amounts of metasomatic magnetite alteration. The magnetite also contains Co, Nb, Sr, Y, and REE compositional zoning (with the latter associated with variations in P and Ca concentrations; Fig. 9). Other elements (e.g., V) gradually change in concentration within the magnetite. The elemental mapping of massive magnetite within Gushan-M samples yielded minor to negligible spatial compositional variations barring minor variations in elements such as V and Ti (Fig. 10).

Some of the magnetite REE analyses yielded values below the LOD, and average REE concentrations calculated using values above the detection limit were used to plot chondrite-normalized REE variation diagrams (Fig. 10). These diagrams indicate that both massive and brecciated magnetite ores are light REE (LREE; La, Ce, Pr, and Nd) enriched, with chondrite-normalized LREE values > 1 and with negligible Eu anomalies. These REE compositions are similar to those of the ore-related porphyritic gabbrodiorite intrusion as well as the dioritic Zhonggu magmatic rocks, all of which are LREE-enriched but are heavy REE (HREE) depleted (Sun et al. 2017; Fig. 11). The magnetite within the iron ore breccias from the Gushan deposit also contains lower concentrations of Mg, Ni, and Zn but higher concentrations of V and Ti than the massive and vein-hosted magnetite.

Iron ore from the Hemushan, Longshan, Baixiangshan, Zhongjiu, and Taipingshan deposits

Magnetite from these deposits is homogeneous during BSE and reflected light imaging (Fig. 6j, k), suggesting it was not metasomatized by late-stage fluids. The magnetite from the Hemushan deposit contains a wide range of Ca, Mg, and Al concentrations and a very narrow range of Cr, Mn, V, Co, Ni, and Zn concentrations. The magnetite from the Zhongjiu deposit is compositionally similar to magnetite from the Hemushan deposit but has a wider range of Ca and Al concentrations and a narrow range in Mn, V, Ti, Co, Ni, Zn, and Ga concentrations (ESM 2; Fig. 7). Magnetite from the

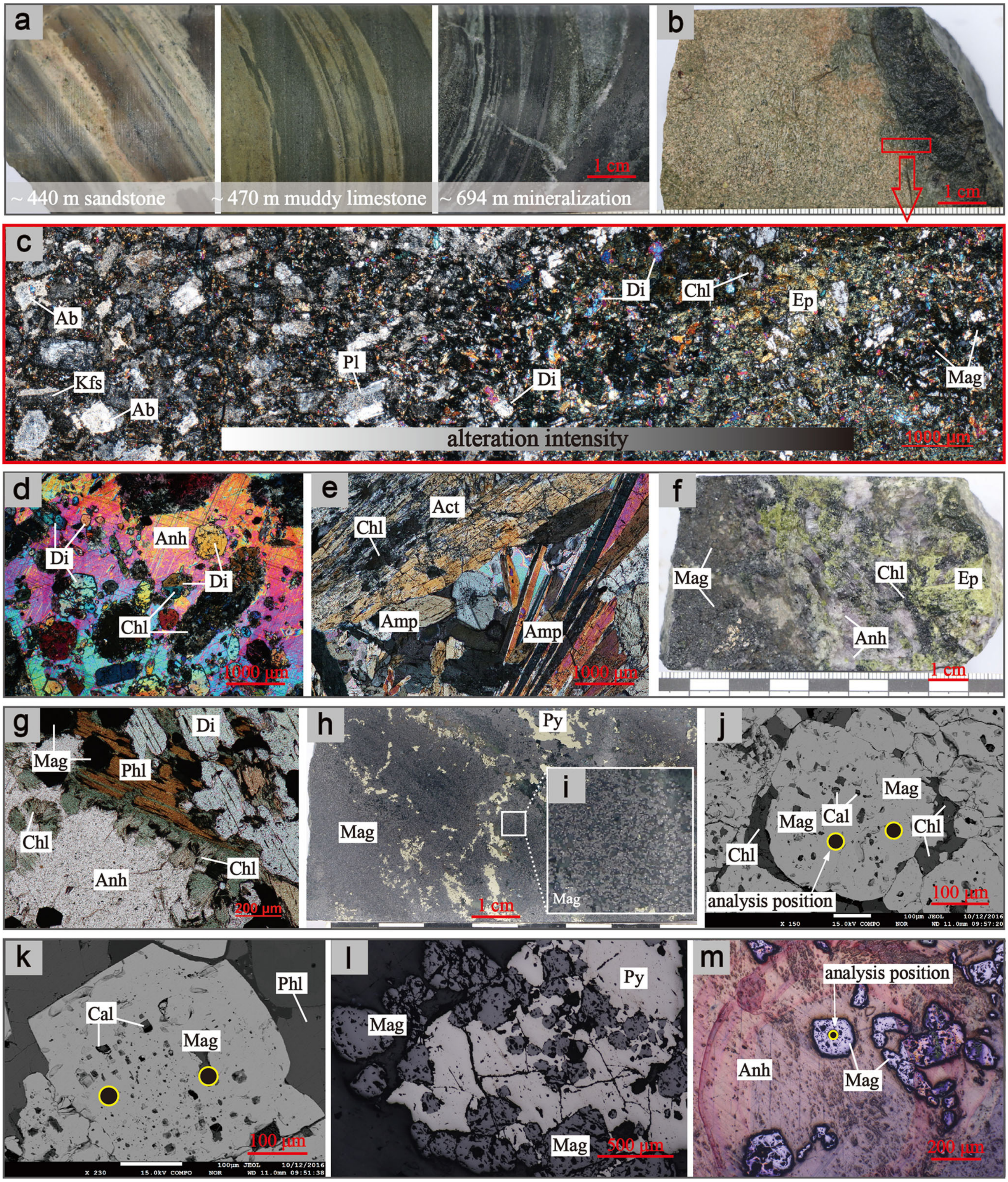

Hemushan, Longshan, Baixiangshan, Zhongjiu, and Taipingshan deposits also generally has a wide range of concentrations of Ca, Mg, Al, Cr, and Zn, but a limited range in Mn, V, Ti, Co, Ni, and Ga concentrations (Fig. 7). Our LA–ICP–MS data indicate that the Hemushan magnetite contains the highest concentrations of Mg and Al of any of the iron ores analyzed as well as having the highest Ca + Al + Mn values (0.2–2 wt%; average 0.9 wt%). Lower Ca + Al + Mn values were obtained for magnetite from the Baixiangshan (0.33–0.98 wt%; average 0.6 wt%), Taipingshan (0.72–0.93 wt%;

◀**Fig. 6** Representative samples from the Zhonggu Fe deposits other than the Gushan deposit. **a** Triassic sedimentary units and associated mineralization within drillcore shown from shallow (~ 440 m) to deep (~ 694 m). **b** Representative sample of diorite showing igneous mineralogy (left) and later albite, chlorite, epidote, and diopside alteration (right). **c** Enlarged mosaic derived from four photomicrographs showing variations in the intensity of alteration (from left to right) taken under cross-polarized light. **d** Early stage diopside altered by chlorite imaged under cross-polarized light. **e** Amphibole–actinolite assemblage altered to chlorite and imaged under cross-polarized light. **f** Photograph of a hand specimen containing a typical mineralization assemblage. **g** Photomicrograph of a thin section of F showing representative mineralogy under plane-polarized light. **h** Photograph of a hand specimen containing disseminated magnetite. **i** Enlarged polished surface showing a representative example of disseminated and fine-grained iron ore. **j** BSE image showing disseminated iron ore and original LA–ICP–MS analysis positions within a sample from the Longshan deposit. **k** BSE images of representative magnetite samples from the Taipingshan deposit. **l** Later pyrite alteration overprinting earlier-formed magnetite. **m** Photomicrograph showing rounded magnetite within anhydrite from the Longshan deposit (reflected light). Abbreviations: Ab = albite; Kfs = K-feldspar, Pl = plagioclase, Di = diopside, Amp = amphibole, Chl = chlorite, Ep = epidote, Act = actinolite, Phl = phlogopite, Mag = magnetite, Py = pyrite, Cal = calcite, Anh = anhydrite

average 0.82 wt%), Longshan (LS-1 0.11–0.76 wt%; average 0.44 wt%), and Zhongjiu (0.35–0.97 wt%; average 0.5 wt%) deposits. The three types of magnetite within the Gushan deposit contain lower Ca, Al, and Mn values than magnetite from the skarn-type deposits described above as well as the anhydrite-associated magnetite.

The anhydrite-hosted magnetite (sample LS-2) contains moderate but variable concentrations of Ca and Al, with the latter lower than that of disseminated magnetite from the Longshan deposit (sample LS-1). Anhydrite-hosted magnetite also contains lower concentrations of Mn than disseminated magnetite, as well as the lowest concentrations of V, Co, and Zn of any magnetite analyzed during this study. This difference is clear in Co/Zn, Mn/Ga, and V/Ga ratio diagrams (Fig. 8).

Discussion

Gushan deposit

Classification of the Gushan deposit

The Gushan deposit was originally described as a porphyry-type iron deposit by Chinese researchers (Ningwu Research Group 1978; Gu and Ruan 1988, 1990). Later, it was classified as an IOCG deposit by Mao et al. (2008) and as a Kiruna-type IOA deposit by Hou et al. (2011). Considerable confusion remains over what exactly constitutes a Kiruna-type iron oxide–apatite deposit (e.g., Gu and Ruan 1988, 1990; Groves et al. 2010; Yuan et al. 2010; Jiang 2015), and Knipping et al. (2015b) suggested that magnetite Cr and V concentrations can be used to distinguish between IOCG and Kiruna-type IOA mineralization. Magnetite containing < 100 ppm Cr and > 500 ppm V is usually associated with Kiruna-type IOA deposits. All three types (brecciated, massive, and vein) of magnetite from the Gushan deposit contain concentrations of V and Cr similar to magnetite from the IOA type locality in Kiruna, Sweden (Knipping et al. 2015b). However, although this diagram can effectively discriminate IOA-type mineralization from other types of mineral deposit, it fails to identify a specific mineral deposit type for the other iron deposits within the Zhonggu iron orefield. This includes the Taipingshan, Zhongjiu, and Baixiangshan deposits, which have samples that are scattered and often plot outside of the porphyry, IOCG, and IOA fields (Fig. 12).

Magnetite from the Gushan deposit is different from that from the Longshan, Hemushan, Baixiangshan, Zhongjiu, and Taipingshan deposits in terms of textures and mineral associations. For example, the Gushan deposit is free of syn-mineralization diopside, amphibole, phlogopite, or chlorite alteration, all of which are present in the other five deposits. The Gushan deposit also contains brecciated and massive ore associated with variable amounts of apatite, an assemblage that is typically found in IOA-type deposits (Hou et al. 2009; Jonsson et al. 2013; Weis 2013). The other five deposits are dominated by fine-grained disseminated magnetite associated with different alteration assemblages. The disseminated magnetite ore in these deposits is associated with zoned alteration, generally focused on a central zone of albite and phlogopite alteration that also contains the highest concentrations of magnetite, contrasting with the alteration-free Gushan deposit. This indicates that although some of the magnetite from these five deposits plots within the Kiruna-type IOA field (Fig. 12), their other characteristics distinguish them from IOA-type deposits.

Genesis of the Gushan IOA deposit

Gushan shares characteristics and geological features with several representative IOA deposits, including the Los Colorados deposit in Chile and the Grängesberg and Kiruna deposits in Sweden (Jonsson et al. 2013; Weis 2013; Knipping et al. 2015b). Geometrically, the Gushan iron deposit is located in a large volcanic crater that controls the bell-shaped nature of the deposit. The edge of the deposit consists of iron ore breccias that are associated with contact-type metamorphism and hornfels (Fig. 5a). These features suggest that the early iron mineralization formed at high temperature. Samples from the Gushan deposit indicate that clinopyroxene and plagioclase were the major fractionating phases during the magmatic evolution of the Gushan porphyritic gabbrodiorite. Magnesium concentrations decrease during the evolution of magmas with these compositions, whereas Fe is not preferentially incorporated into clinopyroxene but will instead continue to increase in

Table 1 Geological features of typical deposits within the Zhonggu iron ore field

	Gushan	Longshan	Baixiangshan	Hemushan	Zhongjiu	Taipingshan
Tonnage/grade	180 Mt Fe/grade 50–56%	90 Mt Fe/grade ~ 45%	190 Mt Fe/grade ~ 45%	80 Mt Fe/grade ~ 45%	80 Mt Fe/grade 45–50%	60 Mt Fe/grade ~ 40%
Ore-bearing intrusions/age	Porphyritic gabbrodiorite/129.2 ± 1.7 Ma	Gabbrodiorite/131.6 ± 1.6 Ma	Diorite/131.0 ± 2.0 Ma	Diorite/131.1 ± 1.9 Ma	Diorite/132.3 ± 2.1 Ma	Monzonite/131.6 ± 1.6 Ma
Depth of ore body	Crops out at surface	− 368 to − 750 m	− 250 to − 800 m	− 200 to − 320 m	− 117 to − 250 m	− 700 to − 950 m
Location of mineralization	Contact between intrusion and T_2h	T_2h; T_2z; contact between intrusion and T_2z	Within intrusion; contact between intrusion and T_2h	Contact between intrusion and T_2z	Contact between intrusion and T_2z	Within intrusion; contact between intrusion and T_2z
Metallogenic age	Unknown	132.26 ± 0.87 Ma (Ar–Ar dating of phlogopite)	134.9 ± 1.1 to 130.7 ± 1.1 Ma (Ar–Ar dating of phlogopite)	132.9 ± 1.1 to 129.1 ± 0.9 Ma (Ar–Ar dating of phlogopite)	Unknown	Unknown
Ore minerals	Magnetite, hematite, specularite, limonite	Magnetite, pyrite, chalcopyrite (jot)	Magnetite, hematite, pyrite, chalcopyrite (jot)	Magnetite, hematite, pyrite, chalcopyrite (jot)	Magnetite, hematite, pyrite	Magnetite, pyrite, chalcopyrite
Iron ore texture/structures	Subhedral–euhedral/massive, vein-hosted, brecciated	Anhedral–subhedral/disseminated, vein, stratiform	Anhedral–subhedral/disseminated, vein, lens-shaped, banded	Anhedral–subhedral/disseminated, vein-hosted	Anhedral–subhedral/disseminated, vein-hosted	Anhedral–subhedral–euhedral/disseminated, vein-hosted
Mineral assemblages	Magnetite–hematite–apatite, magnetite–apatite, hematite–quartz, calcite–chalcedony–kaolinite	Magnetite–pyrite–chalcopyrite, magnetite–phlogopite, epidote–chlorite diopside–anhydrite, quartz–pyrite–calcite	Diopside–tremolite, magnetite–phlogopite–chlorite, magnetite–anhydrite, calcite–kaolinite	Albite–phlogopite–diopside–magnetite, epidote–chlorite–magnetite, epidote–chlorite–anhydrite, quartz–pyrite–calcite	Magnetite–phlogopite–chlorite, epidote–chlorite, calcite–kaolinite	Diopside–anhydrite, magnetite–phlogopite–chlorite, magnetite–pyrite–anhydrite, sericite–calcite
Alteration	Silicification; kaolin, carbonate, and jasper alteration	Albite, diopside, actinolite, epidote, chlorite, carbonate, and kaolin alteration; silicification	Diopside, actinolite, epidote, chlorite, carbonate, kaolin, and iron oxide alteration	Diopside, epidote, chlorite, carbonate, and kaolin alteration; silicification	Feldspar, epidote, chlorite, carbonate, and kaolin alteration	Feldspar, diopsite, epidote, chlorite, sericite, and carbonate alteration
References	Fan et al. (2010), Hou et al. (2010), Sun et al. (2017)	Sun et al. (2017), unpublished data	Yuan et al. (2010), Fan et al. (2011)	Fan et al. (2010), 2011), Sun et al. (2017), Yuan et al. (2010)		

Dates and geological information after Fan et al. (2010), Hou et al. (2010), Sun et al. (2017), Yuan et al. (2010). and our unpublished data

T_2h: Triassic Huangmaqing Formation; T_2z: Triassic Zhongchongcun Formation

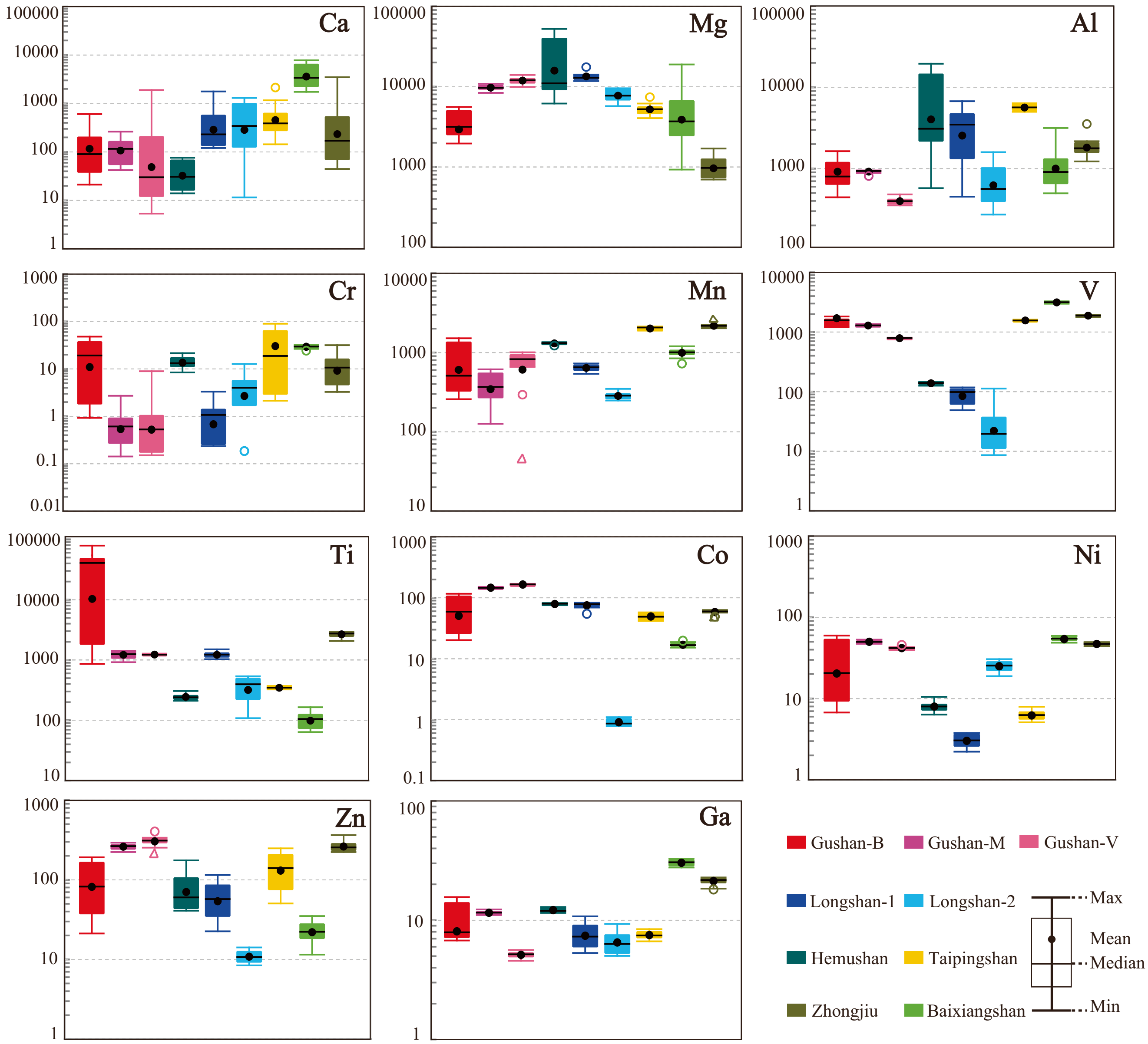

Fig. 7 Box and whisker plots showing variations in magnetite compositions from the six deposits within the Zhonggu orefield. Abbreviations: Gushan-M: massive magnetite ore from the Gushan deposit; Gushan-B: magnetite ore breccia from the Gushan deposit; Gushan-V: vein magnetite ore from the Gushan deposit; Longshan-1: type-1 magnetite from the Longshan deposit; Longshan-2: type-2 anhydrite-hosted magnetite associated with the Longshan deposit

concentration in the evolving liquid. Previous research determined that clinopyroxene cores and rims within the Gushan porphyritic gabbrodiorite record an abrupt change in Fe and Mg content, where Fe contents suddenly decrease and Mg contents suddenly increase (i.e., abrupt reverse zoning; Hou et al. 2011). In addition, plagioclase phenocrysts within this gabbrodiorite are normally zoned and do not record evidence for magma mixing. Hou et al. (2011) suggested that these data indicate the generation of a Fe-rich immiscible melt during the early (i.e., during clinopyroxene fractionation) evolution of the system, a model that is supported by experimental data (Mungall et al. 2018; Hou et al. 2018).

Magnetite from the Gushan iron ore breccia also provides evidence about the processes that formed the deposit. This magnetite contains fairly uniform concentrations of TiO_2 that can be separated into two groups, a low-Ti magnetite group containing < 1 wt% TiO_2 which is similar in composition to massive and vein magnetite as well as magnetite from IOA deposits elsewhere (Jonsson et al. 2013; Weis 2013; Knipping et al. 2015b). The high-Ti group, which contains magnetite with 4–9.5 wt% TiO_2 (ESM 2), is split into two different types of magnetite. The first appears homogeneous during BSE imaging (Fig. 5b), whereas the second type contains small ilmenite lamellae that were analyzed directly by focused beam EPMA and were

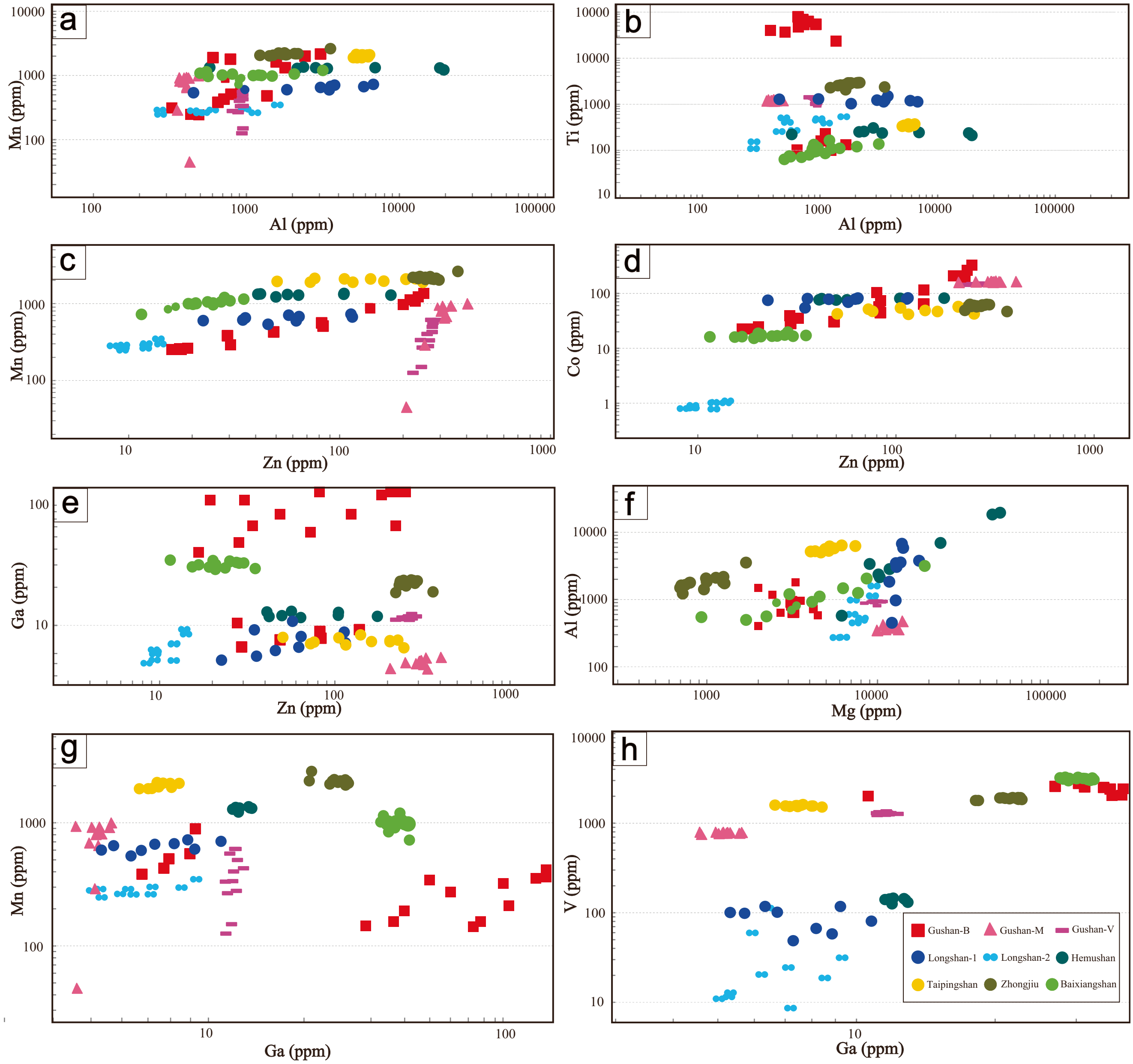

Fig. 8 Diagrams showing the correlations between key element concentrations within magnetite within the Zhonggu orefield: **a** Mn vs. Al; **b** Ti vs. Al; **c** Mn vs. Zn; **d** Co vs. Zn; **e** Ga vs. Zn; **f** Al vs. Mg; **g** Mn vs. Ga; and **h** V vs. Ga

documented using high-magnification BSE imaging (Fig. 5c). The ilmenite likely exsolved from the host magnetite as a result of a decrease in temperature accompanied by a change in fO_2 conditions and is distributed along cleavage or lattice planes within the magnetite, a texture that is common in magmatic iron deposits (Badmatsyrenova and Orsoev 2005). This means that the LA–ICP–MS data obtained for this high-Ti magnetite is a heterogeneous mix of ilmenite and magnetite as a result of the 30-μm diameter of the laser beam. BSE imaging yields an area ratio between ilmenite and magnetite of 1:4 (Fig. 5c), enabling the relative proportions of ilmenite and magnetite to be estimated using this ratio. These relative proportions were converted to volume ratios assuming that the magnetite containing exsolved ilmenite has a cubic form, yielding a magnetite:ilmenite volume ratio of 8:1. This was combined with the average density of magnetite (5.17 g/cm^3) and ilmenite (4.7 g/cm^3) to yield a magnetite:ilmenite mass ratio of 11.36:1. Combining this with the concentration of TiO_2 in ilmenite (50 wt%) and the low-Ti magnetite (1 wt%) in the study area (given that all magnetite in this area contains some Ti) yields an estimated TiO_2 concentration in magnetite of 4.96 wt%. This value is consistent with the homogeneous high-Ti magnetite identified using LA–ICP–MS analysis (ESM 2), indicating that these two subtypes of high-Ti magnetite could have formed by subsolidus exsolution from an originally homogeneous high-Ti magnetite. Titanium concentrations in Fe oxides are thought to be controlled by temperature

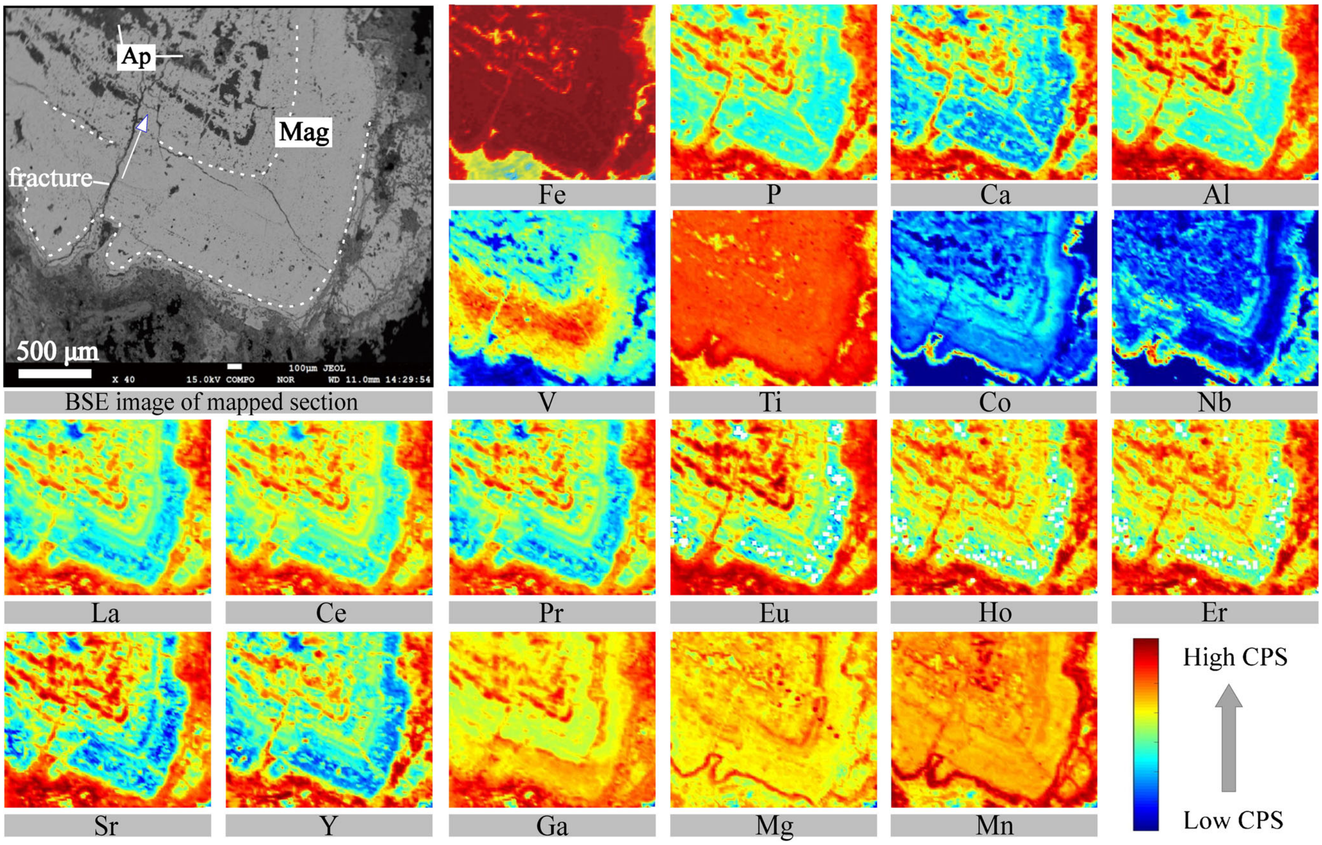

Fig. 9 LA–ICP–MS compositional maps (in counts per second; CPS) showing variations in the composition of magnetite from ore breccias in the Gushan deposit

variations during formation (Dare et al. 2012; Nadoll et al. 2012; Huang et al. 2013), and the calculated high-Ti concentrations of most of the breccia-hosted Gushan magnetite plot within the igneous field of a V vs. Ti magnetite discrimination diagram (Fig. 13a). In comparison, the Gushan-M and Gushan-V magnetite and the remaining Gushan-B magnetite plot in a region of this diagram containing overlapping igneous and hydrothermal fields (Fig. 13a). This suggests that the magnetite from the Gushan deposit is a mix of or a continuum between magmatic and magmatic–hydrothermal magnetite

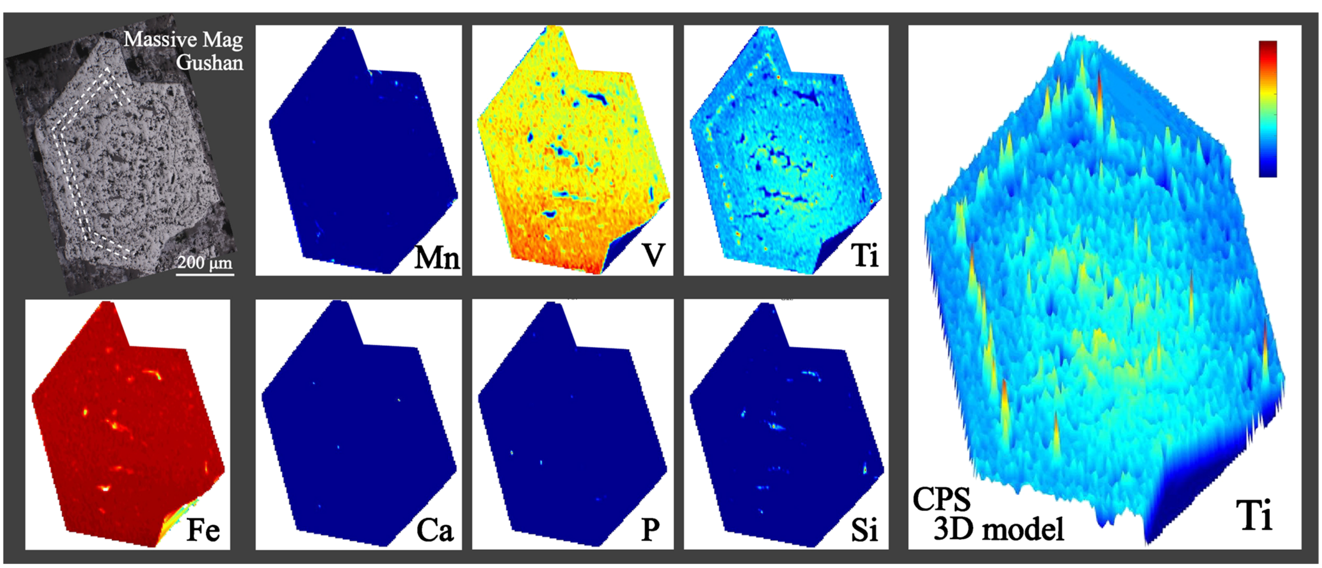

Fig. 10 LA–ICP–MS compositional maps (in counts per second; CPS) showing variations in the compositions of massive magnetite in the Gushan deposit

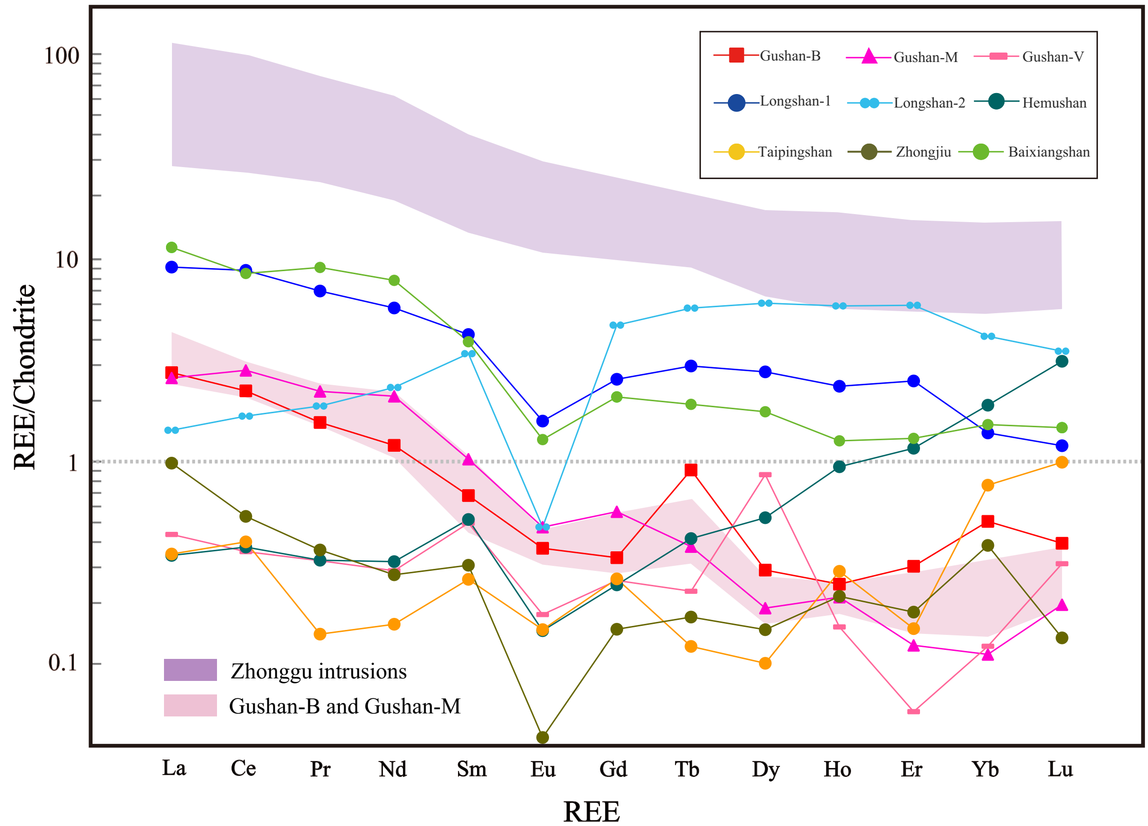

Fig. 11 Chondrite-normalized REE diagram showing variations in the REE composition of magnetite from iron ore deposits in the study area and associated intrusions (Sun et al. 2017), chondrite composition from Sun and McDonough (1989)

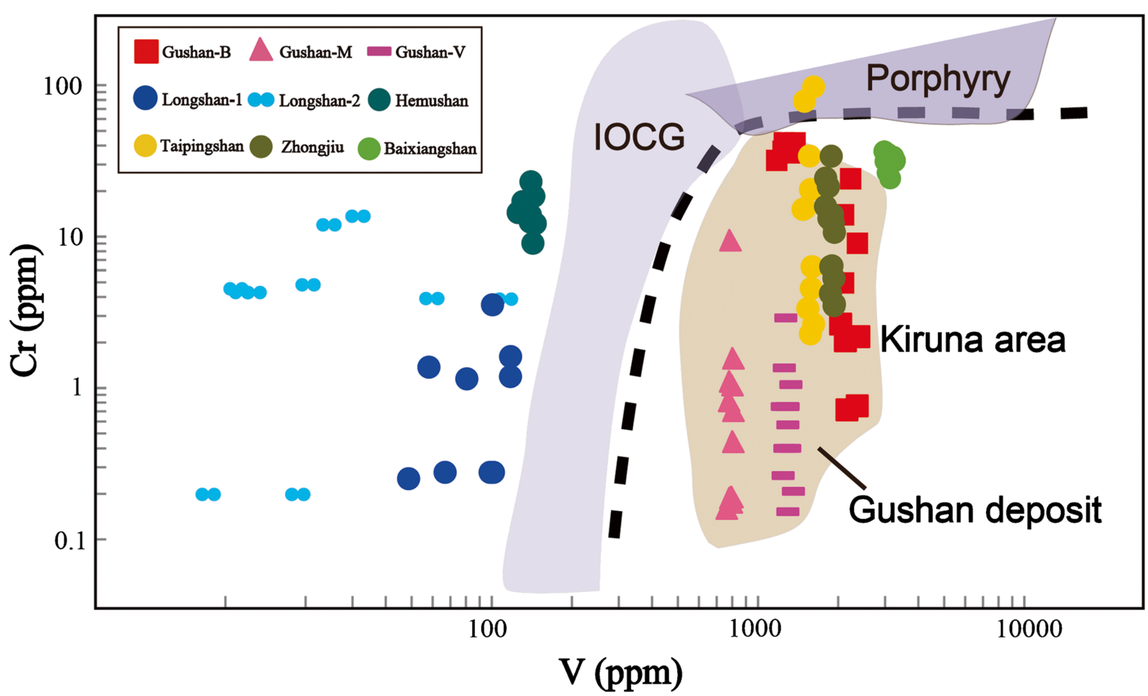

Fig. 12 Diagram showing variations in Cr vs. V for Zhonggu magnetite samples; modified after Knipping et al. (2015b) with typical IOCG magnetite compositions from Carew (2004) and Dare et al. (2014)

end-members. The majority of the massive and vein-hosted magnetite plots in the porphyry and Kiruna fields in the Ca + Mn + Al vs. Ti + V diagram (Fig. 13b), with the majority plotting in the latter. In comparison, magnetite from Gushan-B sample plots within the magmatic Fe–Ti–V deposit and porphyry fields of this diagram (Fig. 13b; Dupuis and Beaudoin 2011; Nadoll et al. 2014b). Li and Xie (1984) reported that magnetite from the Gushan deposit contains inclusions that decrepitate between 350 and 1040 °C, suggesting that earliest magnetite within the deposit formed apparently at temperatures > 900 °C, under orthomagmatic conditions. These high temperatures have been further confirmed by

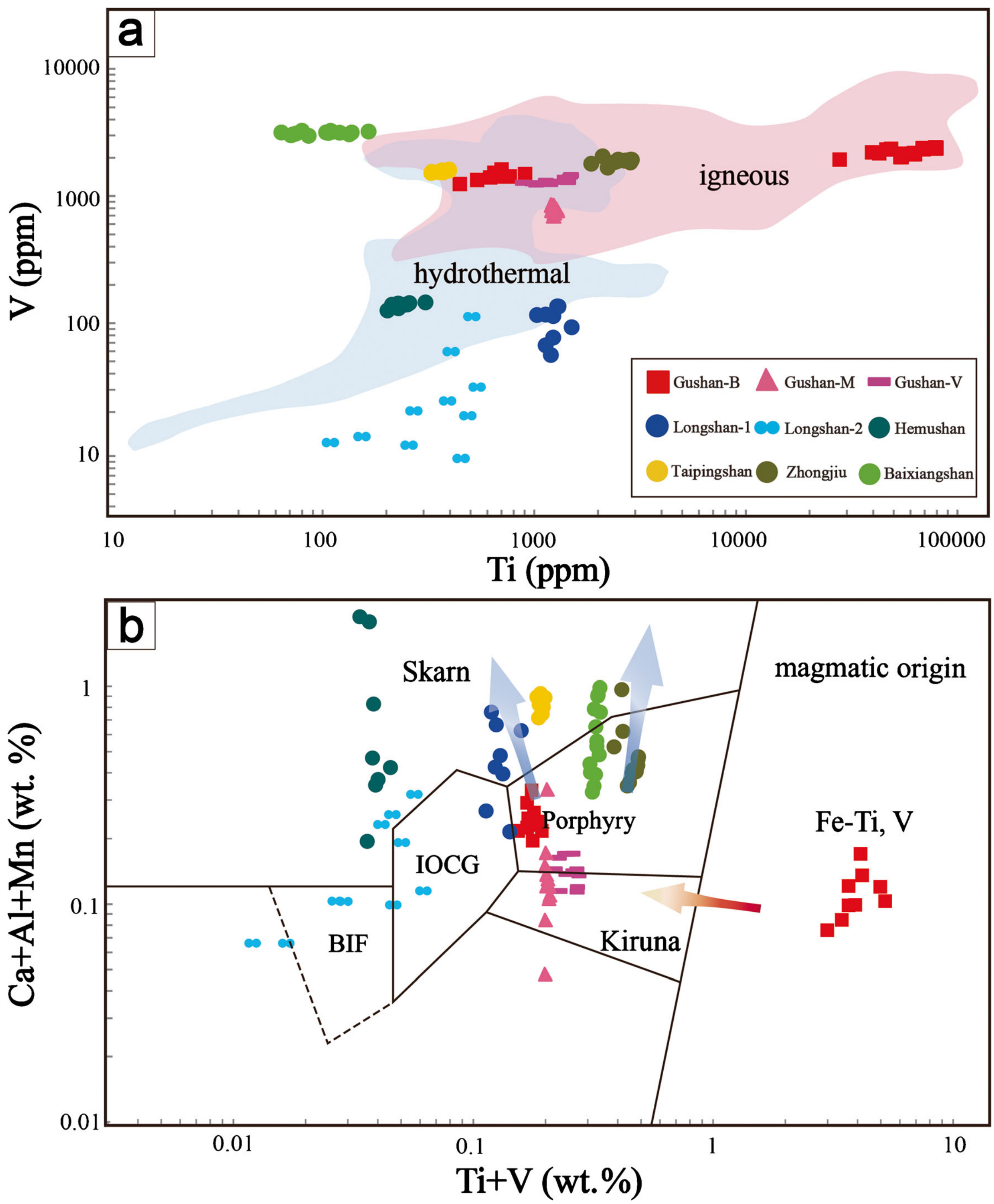

Fig. 13 **a** Diagram showing variations in Ti vs. V for magnetite; red and blue areas indicate igneous and hydrothermal magnetite compositions, respectively (Nadoll et al. 2014b). **b** Diagram showing variations in the Ca + Mn + Al vs. Ti + V compositions of magnetite (Dupuis and Beaudoin 2011); red trend indicates variations in magmatic magnetite compositions (Knipping et al. 2015a)

modeling oxygen isotope fractionation between magnetite and an andesitic parent magma (Zheng 1991; Zhao and Zheng 2003), supporting the presence of both magmatic and magmatic–hydrothermal magnetite in the Gushan deposit.

Formation of the Gushan IOA deposit

The breccias and massive ores from the Gushan deposit are closely spatially related (Fig. 5f). Both massive and brecciated ores are cross-cut by Gushan-V magnetite–apatite ores. Apatite-hosted fluid inclusions in these veins (Fig. 5j) homogenize between 261 and 392 °C (unpublished data), indicating that this magnetite formed under relatively low-temperature conditions. The fluids that formed the Gushan-V magnetite contain P, Ca, and the REE (Yu and Mao 2002) and may have interacted with porous Gushan-B ores. This is supported by the elemental mapping of magnetite that indicates that later fluids moved through and interacted with fractures within this magnetite (Fig. 9). This caused metasomatic alteration around Gushan-B magnetite rims as well as along fractures, decreasing V concentrations but increasing Co, Nb, P, Ca, and REE concentrations, all of which are enriched in the Gushan-V magnetite–apatite ores (Fig. 9). In comparison, the elemental mapping of the massive Gushan magnetite did not identify metasomatic alteration (Fig. 10). Massive magnetite also has spatially uniform concentrations of the majority of the elements barring V and Ti (Fig. 10). These data indicate that, unlike the brecciated ores, the massive ores within the Gushan deposit were not affected by late-stage interaction with the fluids that formed the Gushan-V mineralization. This reflects the impermeable nature of the massive ores within the innermost parts of the Gushan deposit. Variations in V and Ti counts reflect the presence of exsolved ilmenite lamellae within the massive magnetite, similar to the high-Ti magnetite within the Gushan-B iron ore. However, there are far fewer ilmenite lamellae within the Gushan-M magnetite than in the high-Ti Gushan-B magnetite because the former contains lower concentrations of Ti (Fig. 13a). This, combined with (i) the geology of the Gushan deposit; (ii) the plotting of magnetite of the Gushan-M and Gushan-V samples in the overlap region between igneous and hydrothermal fields in Fig. 13a; (iii) the similar concentrations of trace elements such as Mg, Ti, Co, and Mn compared to magnetite within hydrothermal deposits elsewhere within Zhonggu iron orefield; and (iv) the correlations between Ti and Al, Co and Zn, and Al and Mg, supports the interpretation that the formation of the Gushan deposit began with the generation of the magmatic iron ore breccia. Brecciation of these ores was followed by the formation of the massive magmatic–hydrothermal magnetite. The final stage of mineralization within the Gushan deposit was the formation of the lower temperature (hydrothermal) vein Gushan-V magnetite.

Genesis of the Longshan, Hemushan, Baixiangshan, Zhongjiu, and Taipingshan iron deposits

Deposit types

The Longshan, Hemushan, Baixiangshan, Zhongjiu, and Taipingshan deposits were also originally tentatively classified as porphyry-type iron deposits (Ningwu Research Group 1978; Chang et al. 1991; Zhou et al. 2008, 2012). The magnetites within the Longshan, Hemushan, Baixiangshan, Zhongjiu, and Taipingshan deposits all contain similar concentrations of Ti and Co, indicative of formation at similar temperatures (Dare et al. 2012; Nadoll et al. 2012; Huang et al. 2013). Magnetite from the Longshan, Hemushan, Baixiangshan, Zhongjiu, and Taipingshan deposits displays positive correlations between Mn and Al, Ti and Al, Al and Mg, Mn and Zn, and Co and Zn concentrations (Fig. 8). The majority of these magnetites also have similar chondrite-normalized REE patterns except the anhydrite-hosted magnetite, which differs in both slope and Eu anomalies (Fig. 11).

The Baixiangshan deposit is hosted by the Triassic Huangmaqing Formation and a diorite intrusion, whereas the Hemushan, Longshan, Zhongjiu, and Taipingshan deposits are all located along the contact between dioritic intrusions and the Triassic Zhouchongchun Formation (Ningwu Research Group 1978; Chang et al. 1991). The intensity of both hydrothermal alterations and the volume of magnetite within these intrusions increase with proximity to the contact with the surrounding country rock (Fig. 6b, c). The location of orebodies is also closely associated with the distribution of hydrothermal alteration. Magnetite from these deposits is associated with early-formed idiomorphic skarn minerals such as diopside, amphibole, and actinolite that are overprinted by later alteration. Most of the magnetite from these deposits also plots in the skarn field of Fig. 13b although some data from the Longshan (sample LS-1), Baixiangshan, and Zhongjiu deposits plot within the porphyry field of Fig. 13b. This suggests some of the magnetite formed within skarns associated with porphyry systems. In this respect, we note the magnetite from the Vegas Peledas Fe skarn deposit in Argentina (Pons et al. 2009) and the Tengtie Fe skarn deposit in China (Zhao and Zhou 2015) also plot within the skarn and porphyry fields of this diagram. No magnetite from these deposits plots in the fields for IOCG deposit compositions in Cr vs. V diagrams, suggesting that these deposits do not belong to the IOCG deposit type (Dupuis and Beaudoin 2011; Dare et al. 2014). The deposits from the Ningwu Basin also contain low concentrations of Cu and Au, again indicating these are not IOCG deposits, although some magnetite plots within the IOCG field in Fig. 13b. In summary, the geochemical and geological characteristics of the Longshan, Hemushan, Baixiangshan, Zhongjiu, and Taipingshan iron deposits suggest they are skarn deposits formed by magmatic–hydrothermal systems associated with the diorite magmatism.

Genesis of anhydrite-hosted magnetite

The magnetite sample (LS-2) is from thick and massive anhydrite units within the Longshan deposit and contains euhedral–subhedral magnetite hosted by an anhydrite and calcite gangue. This magnetite contains the lowest concentrations of Al (average of 729 ppm), Mn (average of 284 ppm), V (average of 36 ppm), and Co (average of 0.9 ppm) of any of the magnetite within the Zhonggu orefield, as shown in Co vs. Zn, Mn vs. Ga, and V vs. Ga diagrams (Fig. 8). Vanadium concentrations in magnetite can record the evolution of melts or hydrothermal fluids as well as magma replenishment and mixing (McCarthy and Cawthorn 1983; Barnes et al. 2004; Tegner et al. 2006; Namur et al. 2010). Only the V^{3+} ion of vanadium is incorporated into the magnetite crystal lattice (Toplis and Corgne 2002; Bordage et al. 2011; Nadoll et al. 2014a), and increasing amounts are incorporated with progressively more reducing conditions (Toplis and Corgne 2002). The low concentrations of V in the LS-2 magnetite are thus indicative of formation under high fO_2 conditions, consistent with the high fO_2 conditions usually associated with anhydrite generation (Toplis and Corgne 2002). This is consistent with the low-Ti nature of this magnetite, indicating a nonmagmatic origin. The majority of the LS-2 samples ($n = 8$) plot outside the hydrothermal field of a V vs. Ti diagram (Fig. 13a). This indicates that the LS-2 magnetite most likely formed during deposition of the host anhydrite. Sulfate minerals in sample LS-2 are dominantly sedimentary anhydrite, the formation of which was controlled by the temperature and salinity of the sedimentary environment (Freyer and Voigt 2003; Leitner et al. 2013). The anhydrite in sample LS-2 is granular and forms thick and almost monomineralic beds, contrasting sharply with the anhedral hydrothermal anhydrite from the Longshan deposit that is associated with epidote, chlorite, pyrite, and magnetite (Fig. 6f). This type of sedimentary anhydrite formation has been recorded in other locations, including Stassfurt in Germany, Wieliczka in Poland, and Blabberg in Austria (Goldscheider and Bechtel 2009; Leitner et al. 2013). Unusually for sample LS-2, two of the magnetites plot within the hydrothermal field of the V vs. Ti diagram (Fig. 13a), suggesting that some of this magnetite was either altered or reacted with hydrothermal fluids after initial low-temperature formation. This sedimentary to hydrothermal model is supported by the fact that LS-2 magnetite plots in both skarn and BIF fields in a Ca + Mn + Al vs. Ti + V diagram, confirming that this lower grade anhydrite-hosted magnetite mineralization was influenced by both sedimentary and skarn-type processes (Fig. 13b).

Influence of anhydrite formation on the genesis of iron deposits within the Middle–Lower Yangtze River Metallogenic Belt

A thick anhydrite formation crops out throughout the MLYRMB, especially within the Luzong and Ningwu basins (Ningwu Research Group 1978; Chang et al. 1991; Fan et al. 1995; Hou et al. 2010). Previous research has also suggested that this anhydrite may have played a role in the generation of the iron mineralization in this area (Fan et al. 1995; Li et al. 2014; Zhou et al. 2014). Li et al. (2014) suggested that the Triassic anhydrite unit acted as an oxidation barrier and provided elements for the sodic, scapolite, and skarn alteration as well as the Cl^- that enabled the transportation of $FeCl_2$ (Chou and Eugster 1977). However, drill holes that intercepted this evaporite indicate that it could have, moreover, interacted with silicate magmas and hydrothermal fluids, causing the oxidation of Fe^{2+} to Fe^{3+}. This increased the amount of iron within the regional magmas and fluids that then formed the magnetite mineralization (Li et al. 2014). The iron within the majority of these deposits (barring the magmatic Gushan magnetite) was thus sourced from magmatic–hydrothermal systems that likely interacted with anhydrite during metallogenesis (Ningwu Research Group 1978; Li et al. 2014; Zhou et al. 2014). This suggests that some of the Fe skarn deposits in the region may contain a recycled iron component from the sedimentary anhydrite units, although this concept requires further dedicated testing in the future.

Relationships between the Gushan IOA deposit and other Fe deposits within the MLYRMB

The Zhonggu iron orefield formed as a result of regional-scale Early Cretaceous magmatism (132.6 to 129.4 Ma; Fan et al. 2010; Sun et al. 2016, 2017). Phlogopite intergrown with magnetite in the Longshan, Hemushan, and Baixiangshan deposits yielded $^{40}Ar/^{39}Ar$ ages of 134 to 132 Ma (unpublished data; Yuan et al. 2010), slightly younger than the ages of associated intrusions. This magmatism and mineralization was contemporaneous with the second stage (135 to 127 Ma) of magmatism and mineralization elsewhere in the MLYRMB (Sun et al. 2017). The mineralized intrusions within the Zhonggu iron ore field are geochemically similar, were probably derived from similar sources, and probably underwent similar igneous evolutionary processes (Fig. 11; Sun et al. 2017). This suggests that the dioritic magmas within the Zhonggu orefield, including the Gushan porphyritic gabbrodiorite associated with the Kiruna-type IOA mineralization, may have been derived from a single, deep-seated magma source (Ningwu Research Group 1978; Hou et al. 2010; Sun et al. 2017). In addition, Hemushan and Taipingshan magnetites, some magnetite from the Baixiangshan deposit, and the Kiruna-type Gushan-M and Gushan-V magnetite all plot in the overlap region between igneous and hydrothermal fields in Fig. 13a. Magnetite from the Hemushan and Baixiangshan deposits and the LS-1 magnetite from the Longshan deposit also plot between the porphyry and skarn fields in Fig. 13b, whereas the Gushan-M, Gushan-V, and some Gushan-B magnetites plot between the porphyry and Kiruna-type fields in Fig. 13b. All of this suggests that the majority of magnetite in the Zhonggu region formed from skarn-dominated magmatic–hydrothermal systems. The main exception to this is the magmatic Gushan brecciated magnetite. However, the later magmatic–hydrothermal massive and hydrothermal vein magnetite formed from a very similar magmatic–hydrothermal system as the other main deposits in this region. This suggests that the main deposits in the study area record different stages of probably cogenetic magmatic to hydrothermal ore-forming systems.

Conclusions

1. The Gushan iron oxide apatite deposit is a Kiruna-type deposit that contains early-formed high-Ti and high-temperature magmatic brecciated magnetite and later-formed magmatic–hydrothermal massive and hydrothermal vein magnetite mineralization. Early magnetite within the brecciated iron ores was partly overprinted by magmatic–hydrothermal fluids, providing insights into the relative timing of formation of these ores.
2. The Longshan, Hemushan, Baixiangshan, Zhongjiu, and Taipingshan deposits are all skarn-dominated deposits formed by magmatic–hydrothermal systems. The Longshan deposit also contains original sedimentary magnetite hosted by a thick anhydrite unit (sample LS-2) that was overprinted by later low-temperature hydrothermal activity.
3. The geological and geochemical characteristics of the iron ore deposits reflect changing styles of mineralization that record different stages of the similar magmatic–hydrothermal systems that operated within the Zhonggu orefield.

Acknowledgments We thank Georges Beaudoin and Jim Mungall for editorial handling and Adam Simon and two anonymous reviewers for the thorough and constructive reviews that helped to improve our manuscript.

Funding This research was financially supported by funds from the National Key Research and Development Program of China (Grant No. 2016YFC0600209), the Fundamental Research Funds for the Central Universities, the China Academy of Science 'Light of West China' Program, and the National Natural Science Foundation of China (Grant Nos. 41820104007, 41320104003, 41672069, 41702353). The authors gratefully acknowledge the financial support from China Scholarship Council.

References

Ali U, Lawrence TL, Durmus B (1996) Geology, geochemistry, and petrology of the alkaline subvolcanic trachyte-hosted iron deposit in the Karakuz area, northwestern Hekimhan-Malatya, Turkey. Int Geol Rev 38(11):995–1005

Badmatsyrenova R, Orsoev D (2005) Origin of titanomagnetite-ilmenite mineralization, Arsentyev gabbro-syenite massif, Transbaikalia, Russia. Mineral Deposit Research: Meeting the Global Challenge. Springer, Berlin, pp 725–727

Barnes SJ, Maier W, Ashwal L (2004) Platinum–group element distribution in the main zone and upper zone of the Bushveld Complex, South Africa. Chem Geol 208:293–317

Beaudoin G, Dupuis C, Gosselin P, Jébrak M (2007) Application to mineral exploration, Ninth Biennial SGA meeting SGA, Dublin Mineral Chemistry of Iron Oxides 497–500

Bordage A, Balan E, Villiers JP, Cromarty R, Juhin A, Carvallo C, Calas G, Raju PV, Glatzel P (2011) V oxidation state in Fe–Ti oxides by high-energy resolution fluorescence-detected X-ray absorption spectroscopy. Phys Chem Miner 38:449–458

Boutroy E, Dare SA, Beaudoin G, Barnes SJ, Lightfoot PC (2014) Magnetite composition in Ni–Cu–PGE deposits worldwide: application to mineral exploration. J Geochem Explor 145:64–81

Carew MJ (2004) Controls on Cu–Au mineralization and Fe oxide metasomatism in the Eastern Fold Belt, NW Queensland, Australia. PhD thesis, James Cook University

Chang YF, Liu XP, Wu YC (1991) The Copper-Iron Belt of the Lower and Middle Reaches of the Changjiang River. Geological Press, Beijing, pp 1–56 (in Chinese)

Chou IM, Eugster HP (1977) Solubility of magnetite in supercritical chloride solutions. Am J Sci 277(10):1296–1314

Dare SAS, Barnes SJ, Beaudoin G (2012) Variation in trace element content of magnetite crystallized from a fractionating sulfide liquid, Sudbury, Canada: implications for provenance discrimination. Geochim Cosmochim Acta 88:27–50

Dare SAS, Barnes SJ, Beaudoin G, Méric J, Boutroy E, Potvin DC (2014) Trace elements in magnetite as petrogenetic indicators. Mineral Deposita 49:785–796

Dupuis C, Beaudoin G (2011) Discriminant diagrams for iron oxide trace element fingerprinting of mineral deposit types. Mineral Deposita 46:319–335

Fan HY, Li WD, Wang WB (1995) On the relationship between the marine Triassic evaporate horizons and Cu (Au), Fe deposits in the Middle-Lower Yangtze area. Volcanology & Mineral Resources 16: 32–41 (in Chinese with English abstract)

Fan Y, Zhou TF, Yuan F, Zhang LJ, Qian B, Ma L (2010) Geochronology of the diorite porphyrites in Ning-Wu basin and their metallogenic significances. Acta Petrol Sin 26:2715–2728 (in Chinese with English abstract)

Fan Y, Zhou TF, Yuan F, Zhang LJ, Qian B, Ma L, Xie J, Yang XF (2011) Geochronology of the porphyry-like type iron deposits in Ning-Wu basin: Evidence from ^{40}Ar-^{39}Ar phlogopite dating. Acta Geologica Sinica 85(5): 810-820 (in Chinese with English abstract)

Freyer D, Voigt W (2003) Crystallization and phase stability of $CaSO_4$ and $CaSO_4$-based salts. Monatsh Chem 134:693–719

Frietsch R (1978) On the magmatic origin of iron ores of the Kiruna type. Econ Geol 73:478–485

Ghasem N, Majid G (2013) Oxygen isotope and fluid inclusion study of the Sorkhe-Dizaj iron oxide-apatite deposit, NW Iran. Int Geol Rev 55(4):397–410

Goldscheider N, Bechtel TD (2009) Editors' message: The housing crisis from underground—damage to a historic town by geothermal drillings through anhydrite, Staufen, Germany. Hydrogeol J 17(3):491–493

Groves DI, Bierlein FP, Meinert LD, Hitzman MW (2010) Iron oxide copper-gold (IOCG) deposits through Earth history: implications for origin, lithospheric setting, and distinction from other epigenetic iron oxide deposits. Econ Geol 105(3):641–654

Gu LX, Ruan HC (1988) The hydrothermal origin of the Gushan iron ore deposit in Anhui Province. Mineral Deposits 7:21–30 (in Chinese with English abstract)

Gu LX, Ruan HC (1990) Constraints on the precipitation of ores from hydrothermal fluids in two type of iron deposits within the Nanjing-

Wuhu area. Mineral Deposits 9:112–118 (in Chinese with English abstract)
Hitzman MW, Oreskes NO, Einaudi MT (1992) Geological characteristics and tectonic setting of Proterozoic iron oxide (Cu-U-Au REE) deposits. Precambrian Res 58:241–287
Hou T, Zhang ZC, Du YS, Li ST (2009) Geology of the Gushan iron oxide deposit associated with dioritic porphyries, eastern Yangtze craton, SE China. Int Geol Rev 51(6):520–541
Hou T, Zhang ZC, Encarnacion J, Du YS, Zhao ZD, Liu JL (2010) Geochemistry of Late Mesozoic dioritic porphyries associated with Kiruna-style and strata bound carbonate-hosted Zhonggu iron ores, Middle-Lower Yangtze Valley, eastern China: constraints on petrogenesis and iron sources. Lithos 119:330–344
Hou T, Zhang ZC, Kusky T (2011) Gushan magnetite–apatite deposit in the Ningwu basin, Lower Yangtze River Valley, SE China: hydrothermal or Kiruna-type? Ore Geol Rev 43:333–346
Hou T, Charlier B, Holtz F, Veksler I, Zhang ZC, Thomas R, Namur O (2018) Immiscible hydrous Fe–Ca–P melt and the origin of iron oxide-apatite ore deposits. Nat Commun 9:1415
Huang XW, Zhou MF, Qi L, Gao JF, Wang YW (2013) Re–Os isotopic ages of pyrite and chemical composition of magnetite from the Cihai magmatic–hydrothermal Fe deposit, NW China. Mineral Deposita 48:925–946
Huang XW, Boutroy É, Makvandi S, Beaudoin G, Corriveau L, Toni AFD (2018) Trace element composition of iron oxides from IOCG and IOA deposits: relationship to hydrothermal alteration and deposit subtypes. Mineralium Deposita. https://doi.org/10.1007/s00126-018-0825-1
Huberty JM, Konishi H, Heck PR, Fournelle JH, Valley JW, Xu H (2012) Silician magnetite from the Dales Gorge member of the Brockman iron formation, Hamersley Group, Western Australia. Am Mineral 97:26–37
Jiang XJ (2015) The ore genesis of Gushan, Taiping iron deposit in Zhonggu ore field, Anhui, China. Master thesis. 1–84. (in Chinese with English abstract)
Jiang SY, Sun Y, Sun MZ, Bian LZ, Xiong YG, Yang SY, Cao ZQ, Wu YM (2010) Reiterative fault systems and super imposed mineralization in the Jiurui metallogenic cluster district, Middle and Lower Yangtze River mineralization belt, China. Acta Petrol Sin 26(9): 2751–2767 (in Chinese with English abstract)
Jonsson E, Troll VR, Högdahl K, Harris C, Weis F, Nilsson KP, Skelton A (2013) Magmatic origin of giant 'Kiruna-type' apatite-iron-oxide ores in central Sweden. Sci Rep 3(1644):1–8
Knipping JL, Bilenker LD, Simon AC, Reich M, Barra F, Deditius AP, Lundstrom C, Bindeman I, Munizaga R (2015a) Giant Kiruna-type deposits form by efficient flotation of magmatic magnetite suspensions. Geology 43:591–594
Knipping JL, Bilenker L, Simon AC, Reich M, Barra F, Deditius A, W lle M, Heinrich CA, Holtz F, Munizaga R (2015b) Trace elements in magnetite from massive iron oxide-apatite deposits indicate a combined formation by igneous and magmatic-hydrothermal processes. Geochim Cosmochim Acta 171:15–38
Leitner C, Neubauer F, Marschallinger R, Genser J, Bernroider M (2013) Origin of deformed halite hopper crystals, pseudomorphic anhydrite cubes and polyhalite in Alpine evaporites (Austria, Germany). Int J Earth Sci 102(3):813–829
Li BL, Xie YH (1984) Origin, classification and metallogenic model of Ningwu porphyry-type iron deposits. Sci China 1:80–86 (in chinese with English abstract)
Li YH, Duan C, Han D, Chen XW, Wang CL, Yang BY, Zhang C, Liu F (2014) Effect of sulfate evaporate salt layer for formation of porphyrite iron ores in the Middle-Lower Yangtze River area. Acta Petrol Sin 30(5):1355–1368 **(in Chinese with English abstract)**
Liu XM, Gao S, Diwu CR, Ling WL (2008) Precambrian crustal growth of Yangtze craton as revealed by detrital zircon studies. Am J Sci 308:421–468
Lu B, Hu SX, Lin YS, Ye SQ (1990) A discussion on genesis and metallogenic model of Ningwu-type iron deposits. Mineral Deposits 9:14–25 (in chinese with English abstract)
Lundberg B, Smellie JAT (1979) Painirova and Mertainen iron ores: two deposits of the Kiruna iron ore type in northern Sweden. Econ Geol 74:1131–1152
Mao JW, Yu JJ, Yuan SD, Chen YB, Xie GQ, Hou KJ, Xiang JF, Yang ZX (2008) Iron oxide-copper-gold deposits: characteristics, present research situation and ore prospecting. Mineral Deposits 27:267–278 (in chinese with English abstract)
Mao JW, Xie GQ, Duan C, Pirajno F, Ishiyama D, Chen YC (2011) A tectono-genetic model for porphyry-skarn-strata bound Cu-Au-Mo-Fe and magnetite-apatite deposits along the Middle-Lower Yangtze River Valley, eastern China. Ore Geol Rev 43(1):294–314
McCarthy T, Cawthorn RG (1983) The geochemistry of vanadiferous magnetite in the Bushveld Complex: implications for crystallization mechanisms in layered complexes. Mineral Deposita 18:505–518
Mungall JE, Long K, Brenan JM, Smythe D, Naslund HR (2018) Immiscible shoshonitic and Fe-P-oxide melts preserved in unconsolidated tephra at El Laco volcano, Chile. Geology 46(3):255–258
Nadoll P, Mauk JL, Hayes TS, Koenig AE, Box SE (2012) Geochemistry of magnetite from hydrothermal ore deposits and host rocks of the Mesoproterozoic Belt Supergroup, United States. Econ Geol 107: 1275–1292
Nadoll P, Angerer T, Mauk JL, French D, Walshe J (2014a) The chemistry of hydrothermal magnetite: a review. Ore Geol Rev 61:1–32
Nadoll P, Mauk JL, Leveille RA, Koenig AE (2014b) Geochemistry of magnetite from porphyry Cu and skarn deposits in the southwestern United States. Mineral Deposita 50:493–515
Namur O, Charlier B, Toplis MJ, Higgins MD, Liégeois JP, Vander AJ (2010) Crystallization sequence and magma chamber processes in the ferrobasaltic Sept Iles layered intrusion, Canada. J Petrol 51: 1203–1236
Ningwu Research Group (1978) Ningwu porphyry iron ores. Geological Publishing House, Beijing, pp 1–197 (in Chinese)
Nyström JO, Billström K, Henríquez F, Fallick AE, Naslund HR (2008) Oxygen isotope composition of magnetite in iron ores of the Kiruna type in Chile and Sweden. GFF 130:177–188
Pan YM, Dong P (1999) The Lower Changjiang (Yangzi/Yangtze River) metallogenic belt, east central China: intrusion and wall rock-hosted Cu-Fe-Au, Mo, Zn, Pb, Ag deposits. Ore Geol Rev 15:177–242
Paràk T (1975) Kiruna iron ores are not "intrusive-magmatic ores of the Kiruna type". Econ Geol 70:1242–1258
Paràk T (1984) On the magmatic origin of iron ores of the Kiruna type—a discussion. Econ Geol 79:1945–1949
Pollard PJ (2000) Evidence of a magmatic fluid and metal source for Fe-oxide Cu-Au mineralisation. In: Porter TM (ed) Hydrothermal iron oxide copper-gold and related deposits: a global perspectiv. Adelaide, Australian Mineral Foundation, pp 27–41
Pons JM, Franchini M, Meinert L, Recio C, Etcheverry R (2009) Iron skarns of the Vegas Peladas District, Mendoza, Argentina. Econ Geol 104:157–184
Reich M, Simon AC, Deditius A, Barra F, Chryssoulis S, Lagas G, Tardani D, Knipping J, Bilenker L, Alfaro PS, Roberts MP, Munizaga R (2016) Trace element signature of pyrite from the Los Colorados iron oxide-apatite (IOA) deposit, Chile: a missing link between Andean IOA and iron oxide copper-gold systems? Econ Geol 111:743–761
Rhodes AL, Oreskes N (1999) Oxygen isotope composition of magnetite deposits at El Laco, Chile: evidence of formation from isotopically heavy fluids. In Geology and ore deposits of the Central Andes. Society of Economic Geologists, Special Publication 7: 333–351
Rusk B, Oliver N, Brown A, Lilly R, Jungmann D (2009) Barren magnetite breccias in the Cloncurry region, Australia; comparisons to IOCG deposits. 10th Biennial Meeting of the SGA Meeting, Australia, pp 656–658

Sillitoe RH, Burrows DR (2002) New field evidence bearing on the origin of the El Laco magnetite deposit, northern Chile. Econ Geol 97: 1101–1109

Singoyi B, Danyushevsky L, Davidson G, Large R, Zaw K (2006) Determination of trace elements in magnetites from hydrothermal deposits using the LA–ICP–MS technique. SEG Keystone Conference, Denver, USA: CD-ROM

Song XX, Chen YC, Sheng JF, Ai YD (1981) On iron deposits formed from volcanogenic-hypabyssal ore magma. Acta Geol Sin 1:41–55 (in chinese with English abstract)

Sun SS, McDonough WF (1989) Chemical and isotopic systematics of oceanic basalts: implications for mantle composition and processes. Geol Soc Lond, Spec Publ 42:313–350

Sun WA, Jiang XJ, Yuan F, Zhou TF, Hong DL, Gao DM, Liu XB, Liu XM (2016) Geochronology and geochemical characteristics for monzonite in Taiping iron deposit, Zhonggu ore field. Geotecton Metallog 40:1–15 (in chinese with English abstract)

Sun WA, Yuan F, Jowitt SM, Zhou TF, Hollings P, Liu GX, Li XH (2017) Geochronology and geochemistry of the Fe ore-bearing Zhonggu intrusions of the Ningwu Basin: implications for tectonic setting and contemporaneous cu-au mineralization in the Middle–Lower Yangzte Metallogenic Belt. Ore Geol Rev 84:246–272

Tegner C, Cawthorn RG, Kruger FJ (2006) Cyclicity in the main and upper zones of the Bushveld Complex, South Africa: crystallization from a zoned magma sheet. J Petrol 47:2257–2279

Toplis MJ, Corgne A (2002) An experimental study of element partitioning between magnetite, clinopyroxene and iron-bearing silicate liquids with particular emphasis on vanadium. Contrib Mineral Petrol 144:22–37

Tornos F, Velasco F, Morata D, Barra F, Rojo M (2011) The magmatic hydrothermal evolution of the El Laco deposit as tracked by melt inclusions and isotope data. In: Barra F, Reich M, FT (eds) Proceedings of the11th Biennial SGA Meeting. Antofagasta, Chile, pp 443–445

Wang FY, Ling MX, Ding X, Hu YH, Zhou JB, Yang XY, Liang HY, Fan WM, Sun WD (2011) Mesozoic large magmatic events and mineralization in SE China: oblique subduction of the Pacific plate. Int Geol Rev 53(5–6):704–726

Weis F (2013) Oxygen and iron isotope systematics of the Grängesberg Mining District (GMD), central Sweden. Master thesis 1–77

Westhues A, Hanchar JM, Whitehouse MJ, Martinsson O (2016) New constraints on the timing of host-rock emplacement, hydrothermal alteration, and iron oxide-apatite mineralization in the Kiruna District, Norrbotten, Sweden. Econ Geol 111:1595–1618

Westhues A, Hanchar JM, LeMessurier MJ, Whitehouse MJ (2017) Evidence for hydrothermal alteration and source regions for the Kiruna iron oxide-apatite ore (northern Sweden) from zircon Hf and O isotope. Geology 45:571–574

Yang ZJ, Shen ZF, Liang SK, Guo YH (1987) Basement texture and evolution of pre-Sinian in Mid-Lower Yangtze area: bulletin Tianjin institute. Geol Miner Resour 18:13–23 (in chinese with English abstract)

Yang YZ, Wang Y, Ye RS, Li SQ, He JF, Siebel W, Chen FK (2017) Petrology and geochemistry of Early Cretaceous A-type granitoids and late Mesozoic mafic dikes and their relationship to adakitic intrusions in the lower Yangtze River belt, Southeast China. Int Geol Rev 59(1):62–79

Yu JJ, Mao JW (2002) Rare earth elements in apatite from porphyrite iron deposit of Ningwu area. Mineral Deposits 21(1):65–73 (in chinese with English abstract)

Yuan SD, Hou KJ, Liu M (2010) Timing of mineralization and geodynamic framework of iron-oxide-apatite deposits in Ningwu Cretaceous Basin in the Middle-Lower of the Yangtze River, China: constraints from Ar-Ar dating on phlogopites. Acta Petrologica Sinia 26:797–808 (in chinese with English abstract)

Yuan F, Li XH, Zhang MM, Jowitt SM, Jia C, Zheng TK, Zhou TF (2014) Three-dimensional weights of evidence-based prospectivity modeling: a case study of the Baixiangshan mining area, Ningwu Basin, Middle and Lower Yangtze Metallogenic Belt, China. J Geochem Explor 145:82–97

Zhai YS, Yao SZ, Lin XD (1992) Copper and iron deposits in Lower Yangtze River. Geological Press, Beijing (in Chinese)

Zhao ZF, Zheng YF (2003) Calculation of oxygen isotope fractionation in magmatic rocks. Chem Geol 193:59–80

Zhao WW, Zhou MF (2015) In-situ LA–ICP–MS trace elemental analyses of magnetite: the Mesozoic Tengtie skarn Fe deposit in the Nanling range, South China. Ore Geol Rev 65:872–883

Zhao LD, Chen H, Zhang L, Li DF, Zhang WF, Wang CM, Yang JT, Yan XL (2016) Magnetite geochemistry of the Heijianshan Fe–Cu(–Au) deposit in Eastern Tianshan: metallogenic implications for submarine volcanic-hosted Fe–Cu deposits in NW China. Ore Geol Rev 100:422–440

Zheng YF (1991) Calculatio of oxygen isotope fractionation in metal oxides. Geochim Cosmochim Acta 55:2299–2307

Zhou TF, Fan Y, Yuan F (2008) Advances on petrogenesis and metallogeny study of the mineralization belt of the Middle and Lower Reaches of the Yangtze River area. Acta Petrol Sin 24: 1665–1678 (in Chinese with English abstract)

Zhou TF, Fan Y, Yuan F, Zhang LJ, Qian B, Ma L, Yang XF (2011) Geochronology and significance of volcanic rocks in the Ning-Wu Basin of China. Sci China Earth Sci 7:960–971 (in Chinese with English abstract)

Zhou TF, Fan Y, Yuan F, Zhong GX (2012) Progress of geological study in the Middle-Lower Yangtze River Valley metallogenic belt. Acta Petrol Sin 28:3051–3066 (in Chinese with English abstract)

Zhou TF, Fan Y, Yuan F, Wu MA, Zhao WG, Qian B, Ma L, Wang WC, Liu YN, Noel CW (2014) The metallogenic model of Nihe iron deposit in Lu-Zong Basin and genetic relationship between gypsum-salt layer and deposit. Acta Geol Sin 88:562–573 (in Chinese with English abstract)